Submitted to *Journal of the European Ceramic Society*, September 2022. Revised October 2022.

Unlubricated sliding wear of B_4C composites spark-plasma sintered with Si aids and of their reference B_4C monoliths

Victor Zamora [a], Francisco J. Martínez-Vázquez [b], Fernando Guiberteau [a], Angel L. Ortiz [a,*]

[a] Departamento de Ingeniería Mecánica, Energética y de los Materiales, Universidad de Extremadura, 06006 Badajoz, Spain.

[b] Departamento de Física de la Materia Condensada, Universidad de Sevilla, 41080 Sevilla, Spain.

Abstract

Two fully-dense B_4C–SiC composites were fabricated by spark-plasma sintering (SPS) from B_4C+Si powders, one superhard (*i.e.*, ~28.7(8) GPa) with abundant SiC by SPS of B_4C+20vol.%Si at 1400°C and the other ultrahard (*i.e.*, ~35.1(4) GPa) with little SiC by SPS of B_4C+4.28vol.%Si at 1800°C, and their unlubricated sliding wear was investigated and compared with those of the reference B_4C monoliths. It was found that the two B_4C–SiC composites underwent mild tribo-oxidative wear with preferential removal of the oxide tribolayer, with the one SPS-ed at 1400°C from B_4C+20vol.%Si being, despite its lower hardness and greater proneness to form oxide tribolayer, only slightly less wear resistant than the one SPS-ed at 1800°C from B_4C+4.28vol.%Si (*i.e.*, ~$1.0(5)\cdot10^7$ *vs* $1.37(8)\cdot10^7$ (N·m)/mm³). The reference B_4C monolith SPS-ed at 1400°C is comparatively two orders of magnitude less wear resistant (*i.e.*, ~$1.70(6)\cdot10^5$ (N·m)/mm³), attributable to its undergoing severe purely mechanical wear by microfracture-dominated three-body abrasion due to its very poor sintering (*i.e.*, high porosity of ~33.5%), poor grain cohesion, and low hardness (*i.e.*, ~3.1(5) GPa). The reference B_4C monolith SPS-ed at

1800°C, while equally or less hard (*i.e.*, 28.4(9) GPa) and slightly porous (*i.e.*, ~5.3%), is somewhat more wear resistant (~$1.8(3)\cdot10^7$ (N·m)/mm³) than the B_4C–SiC composites, attributable to its undergoing only mild purely mechanical wear by plasticity-dominated two-body abrasion without porosity-induced grain pull-out, but it requires SPS temperatures well above 1400°C. Finally, relevant implications for the ceramics and hard-materials communities with interests in tribological applications are discussed.

Keywords: Boron carbide; Ceramic composites; Sliding wear; Spark-plasma sintering; Super/ultrahard ceramics.

* Corresponding author: Angel L. Ortiz (alortiz@unex.es)

1. Introduction

Owing to their extreme hardness and great lightness, B_4C–based materials, whether monoliths or composites, are currently being intensively investigated for contact mechanical applications, and particularly as ballistic impact armours [1-9] and tribological components (*e.g.*, bearings, valves, seals, dies, nozzles, *etc*.) [1,2,10-17]. One class of these promising B_4C–based materials is that of the B_4C–SiC bi-particulate composites [2,3,18-26], whose microstructure consists of a B_4C matrix toughened by SiC grains. Brittleness is a bane of the B_4C monoliths, motivating widespread interest for the B_4C–based composites [1,2] in which the weak interfaces deriving from the thermo-elastic mismatch result in improved toughness [21,27-33]. SiC is one of the preferred toughening second phases for B_4C because, being also very hard and lightweight, the gain in toughness is accompanied by less loss in hardness and lightness [21].

The B_4C–SiC composites are usually fabricated by solid-state hot pressing (HP) or spark-plasma sintering (SPS) from B_4C+SiC powders [21,23,25,34], and less often by reactive HP or SPS from B_4C+Si+C [35,36] or B_4C+Si powders [37-40]. Reactive sintering is especially appealing because the HP or SPS cycles are comparatively smoother, even more so the more Si aids are used. Thus for example, it has been shown recently that B_4C cannot be fully densified by SPS at 1800°C [40], but that it can be done so using 4.28 vol% Si aids and even at only 1400°C using 20 vol% Si aids [40]. Importantly, while there is a solid understanding of the mechanisms of densification and *in-situ* formation of SiC in these promising composites [40,41], nothing is known so far of their wear behaviour despite this knowledge being needed for their use in tribological applications. Consequently, here we investigated the unlubricated sliding wear, the most typical form of frictional contact, of two representative B_4C–SiC composites SPS-ed from B_4C+Si powders, one with abundant SiC fabricated by SPS at 1400°C from B_4C+20vol.%Si and the other with little SiC fabricated by SPS at 1800°C from B_4C+20vol.%Si, and of their two reference B_4C monoliths SPS-

ed under the same conditions.

2. Experimental Procedure

Commercially available powders (Hönagäs AB, Sweden) of submicrometre B_4C (Grade HD 20) and micrometre Si (Grade AX 05) were used to prepare three powder batches, namely, (*i*) B_4C with 20 vol.% Si, (*ii*) B_4C with 4.28 vol.% Si, and (*iii*) B_4C. Next, they were consolidated by SPS (HP-D-10, FCT Systeme GmbH, Germany) in dynamic vacuum under 75 MPa pressure (applied at 300°C) at the following conditions: (*i*) B_4C+20vol.%Si at 1400°C for 15 min, (*ii*) B_4C+4.28vol.%Si at 1800°C for 10 min, and (*iii*) B_4C at both 1400°C for 15 min and 1800°C for 10 min. The resulting composites and reference monoliths, hereafter termed "Comp-B_4C-20%Si-1400°C", "Comp-B_4C-4.28%Si-1800°C", "Ref-B_4C-1400°C", and "Ref-B_4C-1800°C", respectively, were ground, diamond polished to 0.25-µm finish, and characterised microstructurally by scanning electron microscopy (SEM; Quanta 3D, FEI, The Netherlands) and X-ray diffractometry (XRD; D8 Advance, Bruker AXS, Germany) as well as mechanically by Vickers hardness tests (MV-1, Matsuzawa, Japan) at 9.8 N load. Additionally, their surface roughnesses after polishing were measured by optical profilometry (OP; Profilm 3D, Filmetric, USA).

More importantly, they were also characterised tribologically by unlubricated sliding-wear tests (THT-1000, Anton Paar, Austria) in the ball-on-disk geometry, performed in duplicate at ambient conditions, 40 N load, 10 cm/s linear sliding speed, 2-mm track radius, and 1000 m sliding distance using 6.02 mm diameter diamond-coated SiC counter-balls (Dball G10, Nova Diamant, UK). According to the manufacturer's specifications, these balls are extremely ultrahard (*i.e.*, >80 GPa) and have a very shiny and smooth surface (*i.e.*, roughness less than 20 nm). The as-worn surfaces of the disks were examined by digital optical microscopy (DOM; AM7915MZT-Edge, Dino-Lite, The Netherlands) to inspect the wear damage at macroscopic scale. Also, the wear

debris, if any at all, was collected and characterised microstructurally and chemically by SEM together with energy-dispersive X-ray spectroscopy (EDS; Ultim Max 40, Oxford Instruments, UK). Next, the worn surfaces of the disks were gently cleaned, and re-examined by DOM. Additionally, they were also characterised by OP to compute the worn volumes and thence the specific wear rates (SWRs) and wear resistances, and by optical microscopy (OM; Epiphot 300, Nikon, Japan) and SEM (S-3600 N, Hitachi, Japan) to examine the wear damage at microscopic scale.

Lastly, complementary unlubricated scratch tests were also performed (Revetest RST3, Anton Paar, Austria) at ambient conditions, 5 N load, 1 mm/min scratch speed, and 2 mm scratch distance using a 200-μm radius Rockwell-C diamond tip. The resulting scratches were examined by OM.

3. Results and Discussion

3.1. Microstructure and hardness

Figure 1 shows SEM images representative of the microstructure of the four materials, and their XRD patterns. It can be seen (*i*) that Ref-B_4C-1400°C is very poorly sintered (*i.e.*, ~33.5% porosity) and has a fine-grained mono-particulate microstructure composed essentially only of B_4C (Figs. 1A,E), (*ii*) that Comp-B_4C-20%Si-1400°C is fully sintered and has a fine-grained bi-particulate microstructure composed of boron carbide and abundant β-SiC second phase (Figs. 1B,E), (*iii*) that Ref-B_4C-1800°C is very well but not fully sintered (*i.e.*, ~5.3% porosity) and has a coarser-grained mono-particulate microstructure composed essentially only of B_4C (Figs. 1C,E), and finally (*iv*) that Comp-B_4C-4.28%Si-1800°C is fully sintered and has a coarser-grained bi-particulate microstructure composed of boron carbide and little β-SiC second phase (Figs. 1D,E). It has recently been demonstrated [40] that, unlike the monoliths, the boron carbide phase in the

composites is not B_4C but an isostructure $B_xC(Si)$ that is C-deficient and is doped with Si in the linear chain [40,41], with the C deficiency and Si doping being more pronounced the greater the proportion of Si aids used [40].

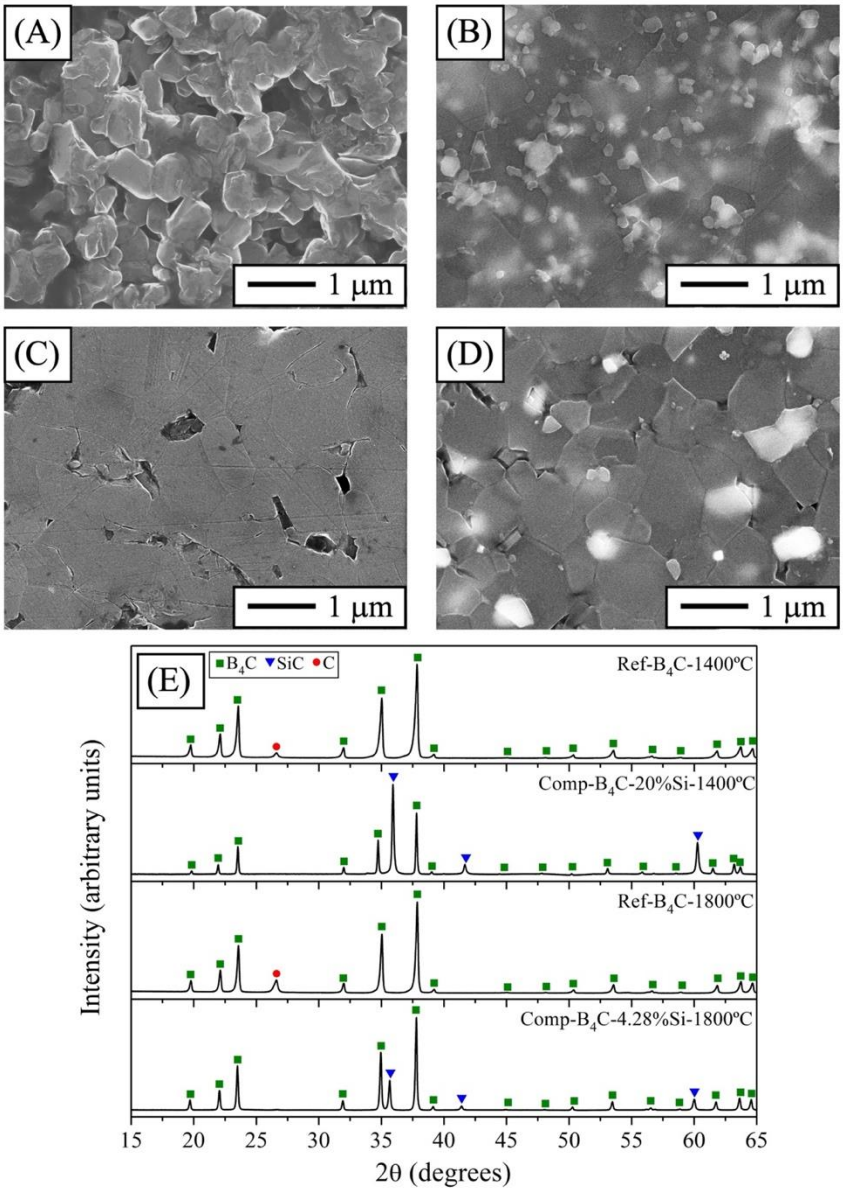

Figure 1. *SEM images representative of the polished, electrochemically etched (1% KOH solution at ~0.03 A/cm² for ~30 s) surface of (A) Ref-B_4C-1400°C, (B) Comp-B_4C-20%Si-1400°C, (C) Ref-B_4C-1800°C, and (D) Comp-B_4C-4.28%Si-1800°C, as well as (E) XRD patterns of these four materials, as indicated. The SEM imaging was done with secondary electrons at 15 kV. In (B) and (D), dark-grey grains are boron carbide and white grains are β-SiC. The XRD patterns were acquired with pure CuKα_1 incident radiation, and were indexed using the PDF2 database. The weak C peak in the XRD patterns of Ref-B_4C-1400°C and Ref-B_4C-1800°C indicates a very minor content (i.e., <1 wt.%) of residual C (impurity of the B_4C and/or taken up during SPS).*

Regarding the surface roughness, the values of the arithmetic mean height (*i.e.*, S_a) of Ref-B_4C-1400°C, Comp-B_4C-20%Si-1400°C, Ref-B_4C-1800°C, and Comp-B_4C-4.28%Si-1800°C are ~0.586, 0.033, 0.106, and 0.009 μm, respectively, and the corresponding values of the root mean square height (*i.e.*, S_q) are ~0.714, 0.041, 0.125, and 0.013 μm. Thus, Comp-B_4C-4.28%Si-1800°C polished the best (*i.e.*, smoothest), followed by Comp-B_4C-20%Si-1400°C, next by Ref-B_4C-1800°C, and finally Ref-B_4C-1400°C polished the worst (*i.e.*, roughest).

The Vickers hardnesses of Ref-B_4C-1400°C, Comp-B_4C-20%Si-1400°C, Ref-B_4C-1800°C, and Comp-B_4C-4.28%Si-1800°C are ~3.1(5), 28.7(8), 28.4(9), and 35.1(4) GPa, respectively. Thus, Ref-B_4C-1400°C is extremely soft, attributable to its very poor sintering. Comp-B_4C-20%Si-1400°C and Ref-B_4C-1800°C are equally superhard (*i.e.*, ≥20 GPa) within the errors (*i.e.*, ~28–29 GPa), but not ultrahard (*i.e.*, ≥30 GPa) because the former contains abundant SiC second phase (which is softer than boron carbide) and the latter pores (which reduce the hardness exponentially [42]). Lastly, Comp-B_4C-4.28%Si-1800°C is indeed ultrahard (*i.e.*, ~35 GPa), attributable to its full densification with very little SiC second phase.

3.2. Wear observations and data

Figure 2 shows DOM images representative of the wear tracks on each material, as well as SEM images and EDS spectra representative of the corresponding wear debris, if any at all. Clearly, Ref-B_4C-1400°C exhibits the greatest abundance of wear debris (Fig. 2A-top), which is concentrated inside and outside its wear track, and by far the widest uncleaned (Fig. 2A-top) and cleaned (Fig. 2A-bottom) wear tracks. Comp-B_4C-20%Si-1400°C and Comp-B_4C-4.28%Si-1800°C also exhibit wear debris (Figs. 2B-top and 2D-top, respectively), although more the former than the latter, which is nonetheless much less abundant than in Ref-B_4C-1400°C and is preferentially located at the outer contours of the wear tracks. Their cleaned wear tracks are also

markedly narrower, but slightly more so that of Comp-B_4C-4.28%Si-1800°C (Fig. 2D-bottom) than that of Comp-B_4C-20%Si-1400°C (Fig. 2B-bottom). The case of Ref-B_4C-1800°C is distinctive in that apparently there is no wear debris, thus exhibiting nearly indistinguishable uncleaned (Fig. 2C-top) and cleaned (Fig. 2C-bottom) wear tracks, which are also the narrowest. Therefore, these observations indicate that Ref-B_4C-1400°C wore the most, followed at a distance by Comp-B_4C-20%Si-1400°C, next by Comp-B_4C-4.28%Si-1800°C, and finally Ref-B_4C-1800°C wore the least. Also importantly, beside differences in wear resistance, there must also be differences in wear modes/mechanisms because Ref-B_4C-1800°C showed no wear debris, and the wear debris of the other three materials differ in abundance, as discussed above, and also in chemical composition and/or morphology. Specifically, the wear debris consists of (*i*) clumps and loose submicrometre B_4C particles in Ref-B_4C-1400°C (Figs. 2E,H-1) but (*ii*) oxide flakes with smooth surface in Comp-B_4C-20%Si-1400°C (Figs. 2F,H-2) and Comp-B_4C-4.28%Si-1800°C (Figs. 2G,H-3), although thinner and smaller in the latter than in the former.

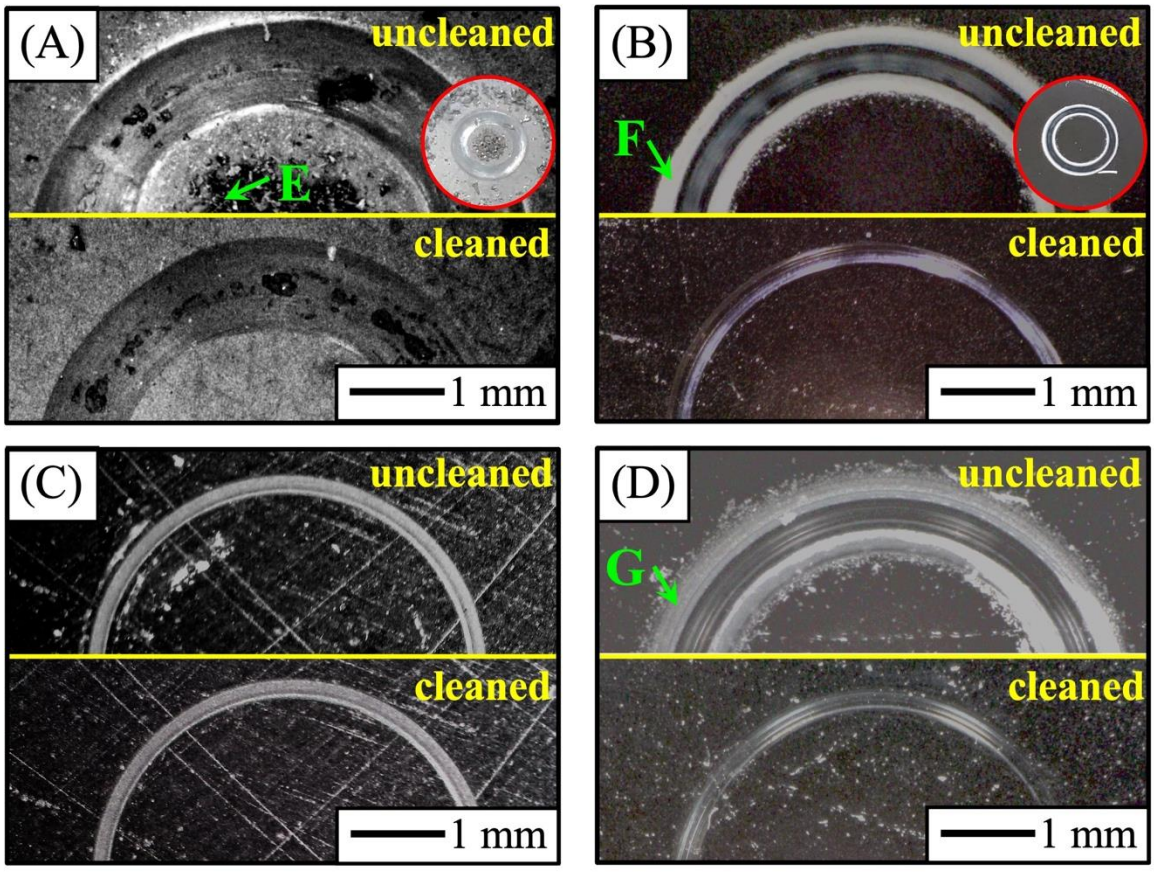

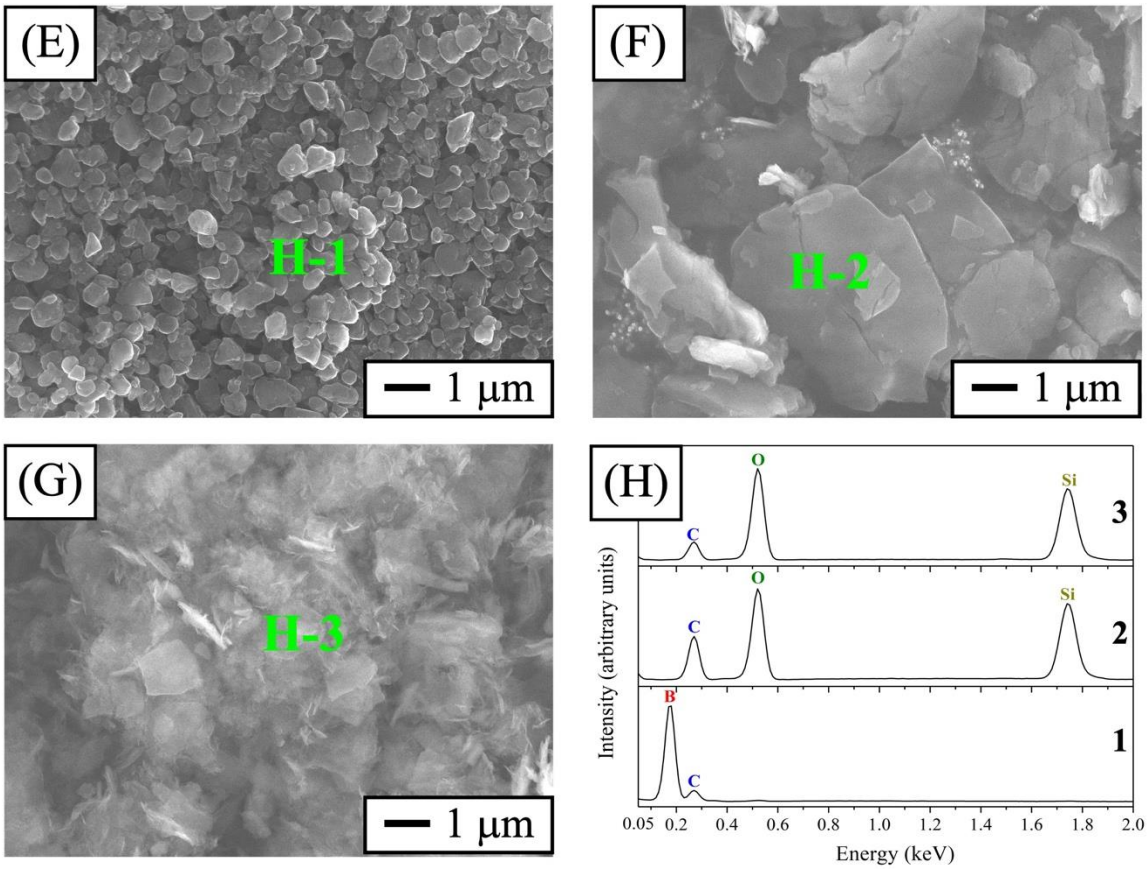

Figure 2. *DOM images representative of the uncleaned (top) and cleaned (bottom) wear tracks of (A) Ref-B_4C-1400°C, (B) Comp-B_4C-20%Si-1400°C, (C) Ref-B_4C-1800°C, and (D) Comp-B_4C-4.28%Si-1800°C at the conclusion of the wear tests (i.e., 1000 m slid). The insets in (A) and (B) show lower-magnification DOM images of the entire wear track (4-cm diameter). SEM images of the wear debris collected from (E) Ref-B_4C-1400°C, (F) Comp-B_4C-20%Si-1400°C, and (G) Comp-B_4C-4.28%Si-1800°C, as well as (H) the corresponding indexed EDS spectra. The SEM imaging was done with secondary electrons at 20 kV, and EDS analyses at 10 kV. The letters E, F, G, H1, H2, and H3 correlate images with each other.*

Figure 3 shows OP 3-D images, and 2-D profiles extracted from them, representative of the cleaned wear tracks in each material. The differences between Ref-B_4C-1400°C and the other three materials are very patent. Certainly, Ref-B_4C-1400°C exhibits by far the widest (*i.e.*, ~930 µm) and deepest (*i.e.*, ~40 µm) wear track (Figs. 3A,E), with a large worn volume (*i.e.*, ~0.236(8) mm^3) and a high SWR (*i.e.*, ~$5.9(2)\cdot10^{-6}$ $mm^3/(N\cdot m)$) that are essentially two orders of magnitude greater than those of the other three materials. Of these, Ref-B_4C-1800°C exhibits the narrowest (*i.e.*, ~245

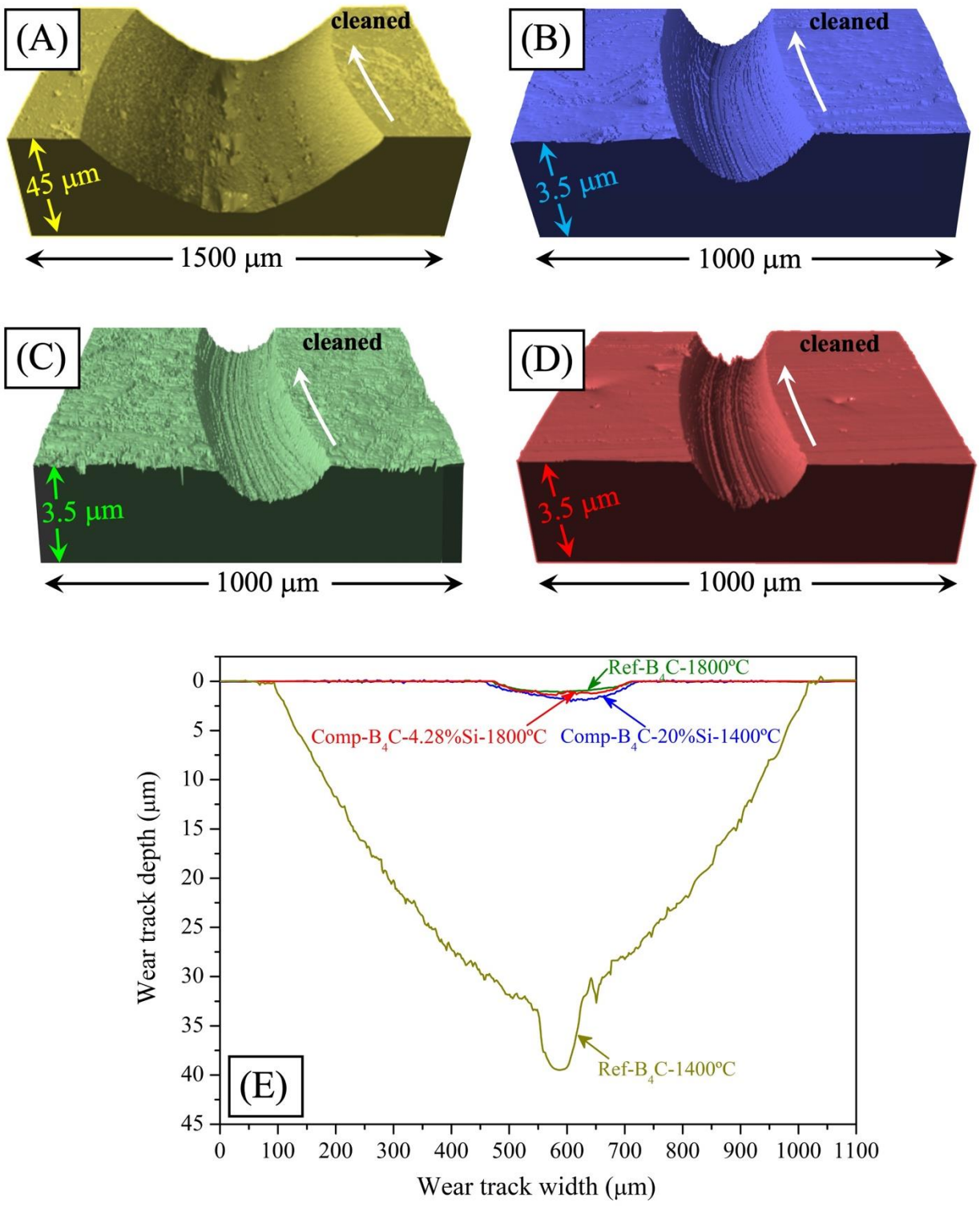

Figure 3. *OP 3-D images representative of the cleaned wear tracks of (A) Ref-B_4C-1400°C, (B) Comp-B_4C-20%Si-1400°C, (C) Ref-B_4C-1800°C, and (D) Comp-B_4C-4.28%Si-1800°C at the conclusion of the wear tests (i.e., 1000 m slid), as well as (E) typical 2-D profiles extracted from them, as indicated. The white arrows in (A)-(D) denote the sliding direction.*

μm) and shallowest (*i.e.*, ~1 μm) wear track (Figs. 3C,E), and therefore the lowest worn volume (*i.e.*, ~0.0023(4) mm³) and SWR (*i.e.*, ~5.8(9)·10^{-8} mm³/(N·m)). Comp-B_4C-4.28%Si-1800°C exhibits the second narrowest (*i.e.*, ~250 μm) and shallowest (*i.e.*, ~1.4 μm) wear track (Figs. 3D,E), with a slightly greater worn volume (*i.e.*, ~0.0029(2) mm³) and SWR (*i.e.*, ~7.3(4)·10^{-8} mm³/(N·m)) than Ref-B_4C-1800°C. And lastly, Comp-B_4C-20%Si-1400°C exhibits an even slightly larger (*i.e.*, ~280 μm × ~2 μm) wear track (Figs. 3B,E), as also are both its worn volume (*i.e.*, ~0.005(2) mm³) and SWR (*i.e.*, ~1.1(4)·10^{-7} mm³/(N·m)). Therefore, the OP observations and data confirm quantitatively that the ranking of wear resistance is Ref-B_4C-1800°C (*i.e.*, ~1.8(3)·10^7 (N·m)/mm³) > Comp-B_4C-4.28%Si-1800°C (*i.e.*, ~1.37(8)·10^7 (N·m)/mm³) > Comp-B_4C-20%Si-1400°C (*i.e.*, ~1.0(5)·10^7 (N·m)/mm³) ⋙ Ref-B_4C-1400°C (*i.e.*, ~1.70(6)·10^5 (N·m)/mm³).

3.3. Wear modes and mechanisms

Figures 4-7 show OM and SEM/EDS images representative of the wear-induced macro- and micro-damage in each material. The great differences of severity and patterns of damage between Ref-B_4C-1400°C and the other three materials are again very evident. Certainly, Ref-B_4C-1400°C exhibits widespread disruption of its surface and subsurface, with wholesale material removal (Fig. 4A) in the form of (*i*) grain pull-out more (Fig. 4B) or less (Fig. 4C) copious everywhere and (*ii*) ejection of large chunks of grains (Fig. 4D) in the central region (where the wear stresses are greater). Therefore, the wear patterns (Fig. 4) and the great amount of wear debris (Fig. 2A-top) indicate that Ref-B_4C-1400°C wore, purely mechanically, predominantly by microfracture-dominated three-body abrasion [43], with the abrasive being the abundant ultrahard B_4C particles/clods dislodged. On the contrary, the other three materials exhibit much less worn surface (Figs. 5-7), comparatively very intact, but especially Ref-B_4C-1800°C (Fig. 6), followed by Comp-B_4C-4.28%Si-1800°C (Fig. 7), and lastly Comp-B_4C-20%Si-1400°C (Fig. 5).

Specifically, they display discernible scratches, typical of plastic grooves, parallel to the sliding direction, but these are less abundant and shallower in Ref-B_4C-1800°C (Fig. 6A), followed by Comp-B_4C-4.28%Si-1800°C (Fig. 7A), and lastly Comp-B_4C-20%Si-1400°C (Fig. 5A). Moreover, this last is the only one of the three that shows signs of minor microfracture-induced grain pull-out (Figs. 5B,C). Importantly, all these observations show that, unlike Ref-B_4C-1400°C, the other three materials possess sufficient grain cohesion under frictional forces, and also that the residual porosity of Ref-B_4C-1800°C was not a source for relevant grain pull-out.

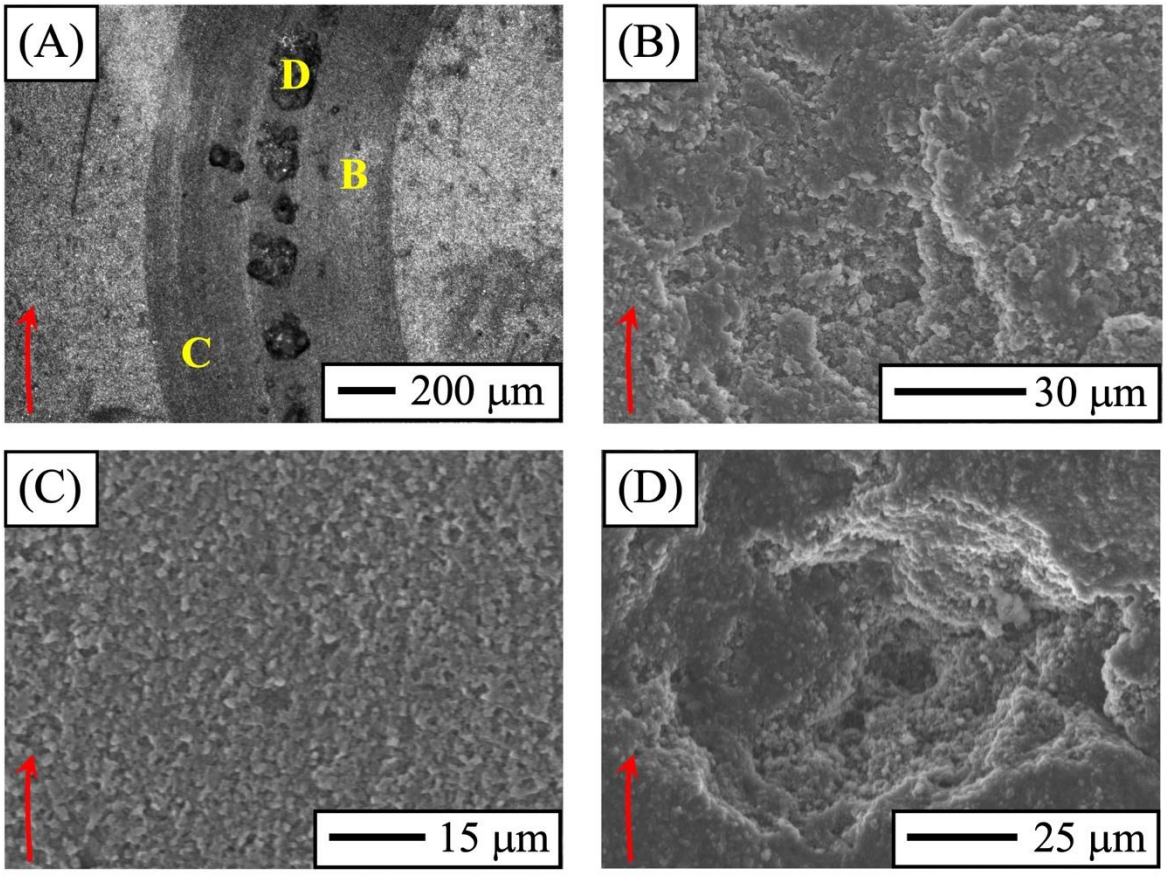

Figure 4. *(A) OM and (B-D) SEM images showing the wear damage at the macro- and micro-scales in Ref-B_4C-1400°C at the conclusion of the wear tests (i.e., 1000 m slid) after cleaning the worn surface. SEM imaging was done with secondary electrons at 15 kV. The red arrows denote the sliding direction. The letters B, C, and D in (A) correlate images with each other.*

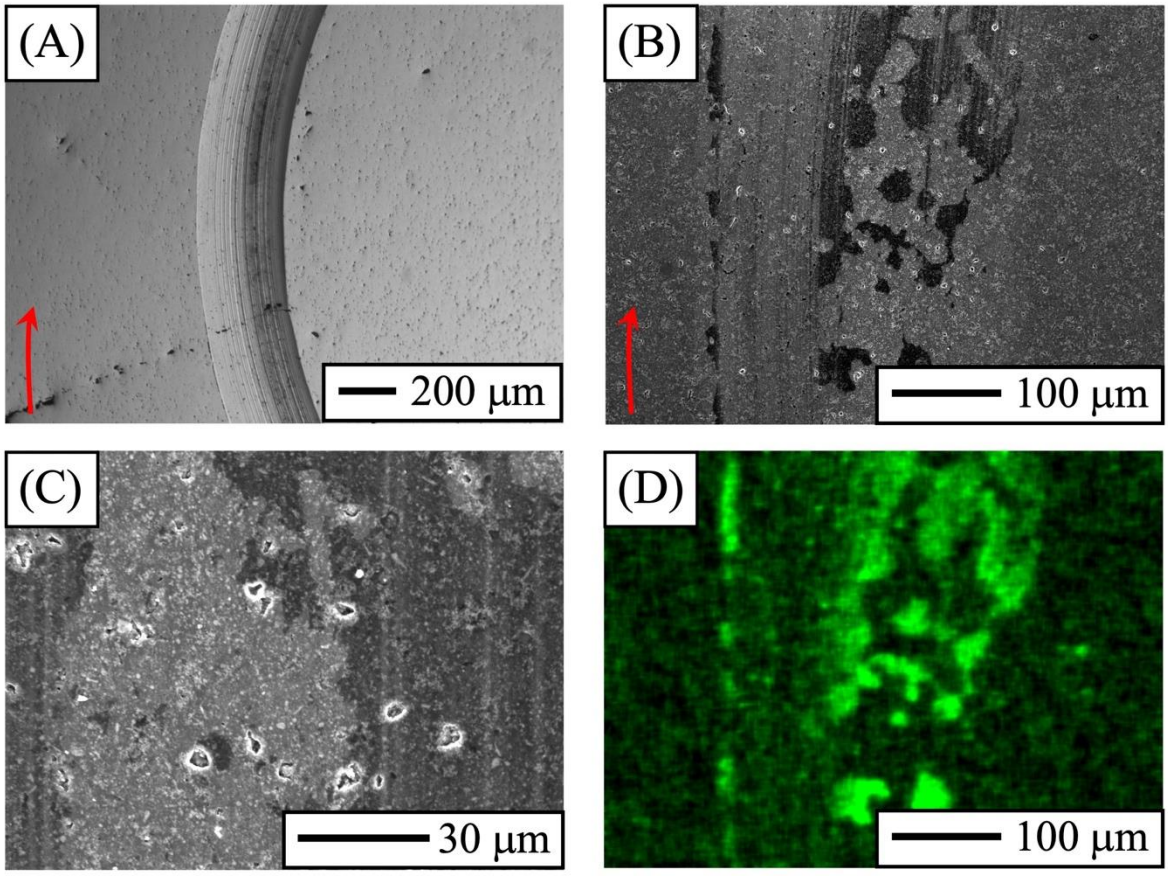

Figure 5. *(A) OM and (B-C) SEM images representative of the wear damage at the macro- and micro-scales in Comp-B_4C-20%Si-1400°C at the conclusion of the wear tests (i.e., 1000 m slid) after cleaning the worn surface. (D) EDS elemental composition map of O inside and outside the wear track. SEM imaging was done with secondary electrons at 15 kV, and EDS mapping also at 15 kV. The red arrows denote the sliding direction.*

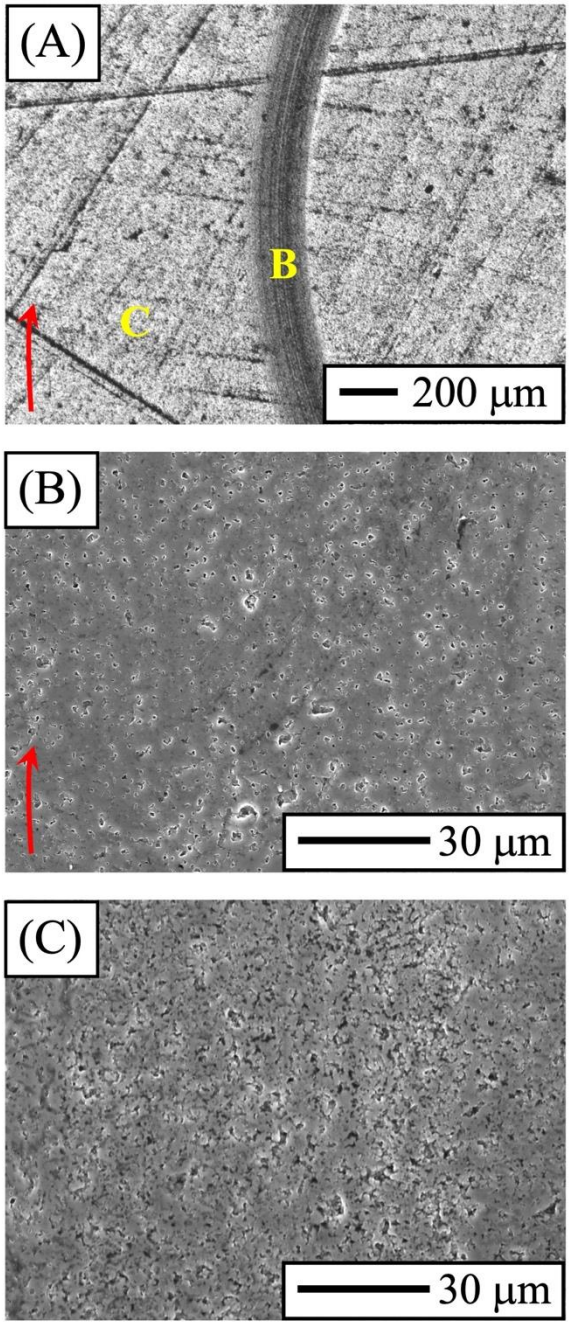

Figure 6. *(A) OM and (B) SEM image representative of the wear damage at the macro- and micro-scales in Ref-B_4C-1800°C at the conclusion of the wear tests (i.e., 1000 m slid) after cleaning the worn surface. (C) SEM image representative of the surface of Ref-B_4C-1800°C outside the wear track showing that the pitted zones in (B) consist of pores, not grains pulled-out during the wear tests. SEM imaging was done with secondary electrons at 15 kV. The red arrows in (A)-(B) denote the sliding direction.*

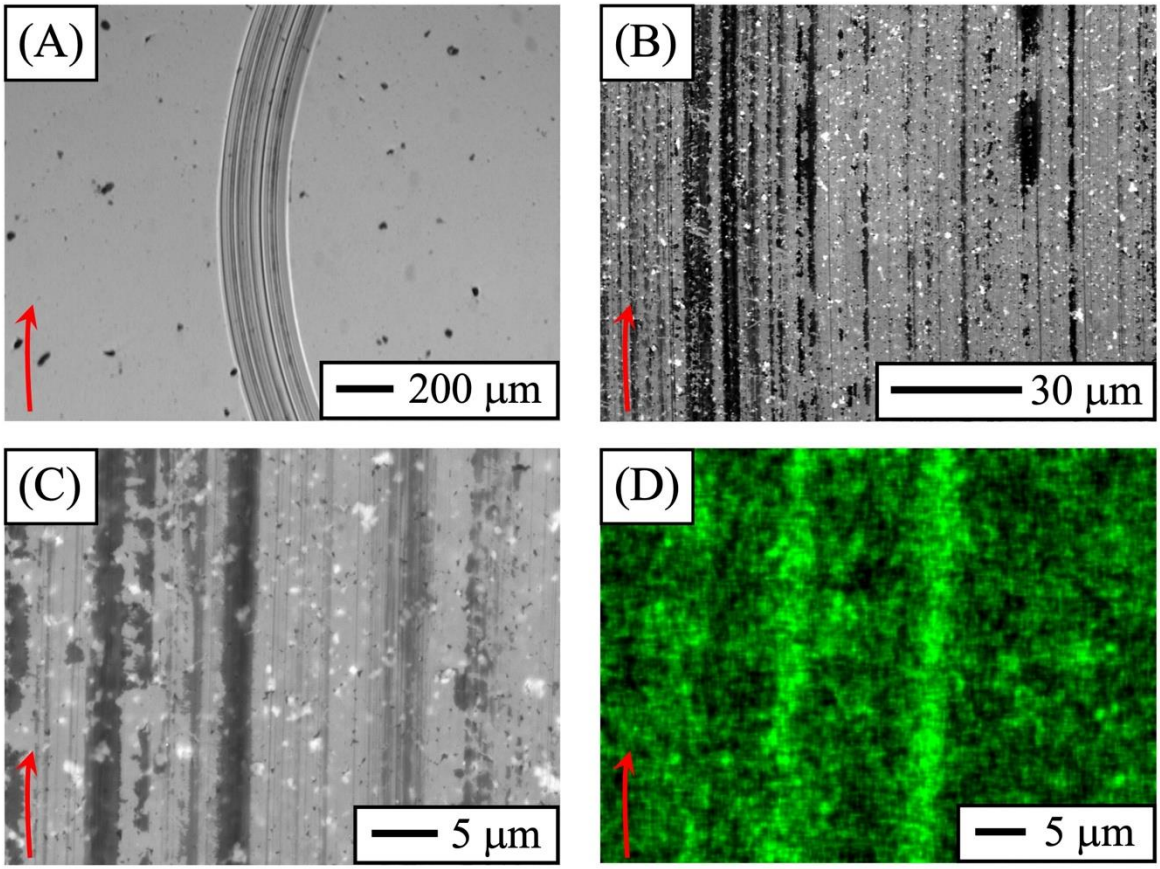

Figure 7. *(A) OM and (B-C) SEM images representative of the wear damage at the macro- and micro-scales in Comp-B_4C-4.28%Si-1800°C at the conclusion of the wear tests (i.e., 1000 m slid) after cleaning the worn surface. (D) EDS elemental composition map of O inside the wear track. SEM imaging was done with secondary electrons at 15 kV, and EDS mapping also at 15 kV. The red arrows denote the sliding direction.*

It can also be seen that the composites exhibit discontinuous oxide tribolayers, apparently thicker and more extensive in Comp-B_4C-20%Si-1400°C (Fig. 5D) than in Comp-B_4C-4.28%Si-1800°C (Fig. 7D), but not the monoliths (Figs. 4 and 6). This is consistent with the types of the wear debris collected in each material. Certainly, in the composites there were oxide flakes (Figs. 2F,H-2 and 2G,H-3) because they are chipped-off tribolayer areas. In Ref-B_4C-1400°C, these were B_4C (Fig. 2H-1) because no oxide tribolayers were formed, and in Ref-B_4C-1800°C there simply was no wear debris (Fig. 2C-top). Therefore, it is evident that the frictional heating generated during the wear tests in air oxidized the contact surface of the composites but not of the monoliths,

which is attributable to the Si present in their microstructures (as SiC grains and Si dopant in the boron carbide grains), and that the oxide tribolayers eventually partially delaminated or spalled. This is indeed the principal cause of material loss in the composites. But importantly, because most of this oxide wear debris was expelled out of the contact zone (Figs. 2B-top and 2D-top), it caused only limited three-body abrasion.

Therefore, the wear patterns (Figs. 5-7) and the observations (Figs. 2B-D) and analyses (Figs. 2F-H) of the wear debris indicate that Ref-B_4C-1800°C, Comp-B_4C-4.28%Si-1800°C, and Comp-B_4C-20%Si-1400°C wore, in that order of from less to more, by different modes/mechanisms and differently from Ref-B_4C-1400°C. Certainly, Ref-B_4C-1800°C did so by purely mechanical wear in the form of plasticity-dominated two-body abrasion [43], with the abrasive being the contact asperities, while the composites did so by tribo-oxidation, which is a combination of mechanical wear and oxidative wear [43] (whose relative importance is expected to vary with increasing sliding distance). Specifically, their wear initially occurred by plasticity-dominated two-body abrasion until the oxide tribolayers were formed, and then the tribolayers wore predominantly by microfracture-dominated two-body abrasion, dictating the onset of an additional slight three-body abrasion (likely dominated by microfracture for the still-remaining tribolayer and by plasticity for the bare worn surface). Notwithstanding the above, tribo-oxidation only caused mild wear, lesser in Comp-B_4C-4.28%Si-1800°C than in Comp-B_4C-20%Si-1400°C (*i.e.*, ~$7.3(4)\cdot10^{-8}$ mm³/(N·m) *vs* ~$1.1(4)\cdot10^{-7}$ mm³/(N·m)) due to its greater hardness and lesser oxidation.

3.4. Correlation wear resistance and Vickers hardness

Figure 8 shows the wear resistance as a function of Vickers hardness for the four materials. It can be seen (*i*) that Ref-B_4C-1400°C is by far, given its super-low hardness (*i.e.*, ~3.1(5) GPa),

the least wear resistant (*i.e.*, ~1.70(6)·10^5 (N·m)/mm³) and that it underwent severe wear [43,44], (*ii*) that Ref-B_4C-1800°C is the most wear resistant (*i.e.*, ~1.8(3)·10^7 (N·m)/mm³) despite not being the hardest (*i.e.*, ~28.4(9) GPa) and that it underwent mild wear [43,44], and (*iii*) that Comp-B_4C-20%Si-1400°C and Comp-B_4C-4.28%Si-1800°C are slightly less wear resistant (*i.e.*, ~1.0(5)·10^7 and 1.37(8)·10^7 (N·m)/mm³, respectively) than Ref-B_4C-1800°C despite the former being equally hard (*i.e.*, ~28.7(8) GPa) and the latter the hardest (*i.e.*, ~35.1(4) GPa) and that they also underwent mild wear [43,44]. Therefore, it is clear that Vickers hardness alone is not a reliable predictor of the wear performance of these materials, which in principle may appear counter-intuitive because the conventional belief is that the harder a material is the less it wears.

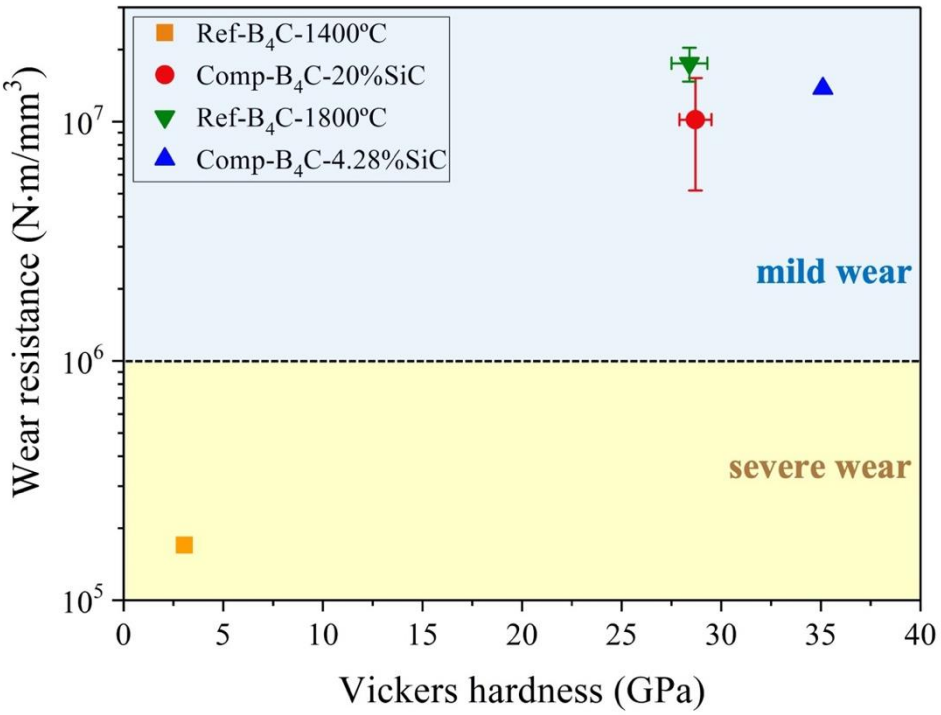

Figure 8. *Wear resistance of Ref-B_4C-1400°C, Comp-B_4C-20%Si-1400°C, Ref-B_4C-1800°C, and Comp-B_4C-4.28%Si-1800°C as a function of their Vickers hardness, as indicated. The regimes of severe and mild wear are distinguished.*

Underlying the above is the fact that wear occurred by different modes and/or mechanisms. Certainly, Ref-B_4C-1400°C wore by microfracture-dominated three body abrasion, in brittle mode, so it was its very poor sintering which conditioned both its super-low wear resistance and its super-

low Vickers hardness. Ref-B_4C-1800°C wore, however, by plasticity-dominated two-body abrasion, in "ductile" mode, so that it was the intrinsic ultra-high hardness of the B_4C grains which dictated its super-high wear resistance. Thus, its ~5.3% porosity reduced its Vickers hardness from ~41(1) GPa[1] to ~28.4(9) GPa, but did not significantly affect its wear resistance. Lastly, Comp-B_4C-20%Si-1400°C and Comp-B_4C-4.28%Si-1800°C wore tribo-oxidatively, more so the former than the latter, and therefore they did so faster than expected according to their Vickers hardness, but still mildly, because their wear resistance was conditioned by the inferior mechanical properties of oxide tribolayers. This proneness to oxidation of the composites could, however, be beneficial for their use in tribological applications where B_4C monoliths undergo active oxidation.

The importance of the oxidative wear was further confirmed by complementary unlubricated single-pass scratch tests. Figure 9 shows OM images representative of the scratches in each material illustrating the relative damage susceptibilities under purely mechanical wear. It can be deduced from the width of the scratch tracks that the scratch resistance follows the order Comp-B_4C-4.28%Si-1800°C (*i.e.*, ~18.5(4) µm; Fig. 10D) > Ref-B_4C-1800°C (*i.e.*, ~22.0(5) µm; Fig. 10C) > Comp-B_4C-20%Si-1400°C (*i.e.*, ~24.9(5) µm; Fig. 10B) ⋙ Ref-B_4C-1400°C (*i.e.*, ~89(1) µm; Fig. 10A), demonstrating that in the absence of oxidative wear Comp-B_4C-4.28%Si-1800°C is, given its greater Vickers hardness, the one that abrades the least.

3.5. Final considerations

The results of the present study may have important implications. First, highly durable (*i.e.*, 10^7 (N·m)/mm³) B_4C–based tribo-components can be fabricated by SPS at only 1400°C if sufficient Si aids are used (*i.e.*, 20 vol.%), which are nearly as wear resistant as other B_4Cs SPS-ed under

[1]It has been demonstrated that Vickers hardness of B_4C monoliths decays exponentially with a rate constant of ~7 due to the residual porosity [42].

more demanding conditions [45-47] and much more affordable to fabricate and/or potentially scalable than other hard ceramics widely used today in tribological applications (*e.g.*, SiC, Si_3N_4, Al_2O_3, *etc*.). Certainly, when also tested tribologically under 40 N load, a fully-dense B_4C composite SPS-ed at 1800°C with 7 vol.% Ti-Al exhibited a SWR of ~$3.1 \cdot 10^{-8}$ mm³/(N·m) [45], a near-fully dense (99%) B_4C monolith SPS-ed at 2100°C a SWR of ~$3.8 \cdot 10^{-8}$ mm³/(N·m) [45], a fully-dense B_4C composite SPS-ed at 1850°C with 5 vol.% Ti-Al a SWR of ~$5.2 \cdot 10^{-8}$ mm³/(N·m) [46], and a fully-dense B_4C composite SPS-ed at 1800°C with 20%vol.% $MoSi_2$ a SWR of ~$3.73 \cdot 10^{-8}$ mm³/(N·m) [47]. Also, the proneness of the B_4C–SiC composites to form passivating layers could favour their use in tribological applications where the B_4C monoliths undergo active oxidation. They therefore deserve further study under an ample set of possible engineering-relevant wear conditions.

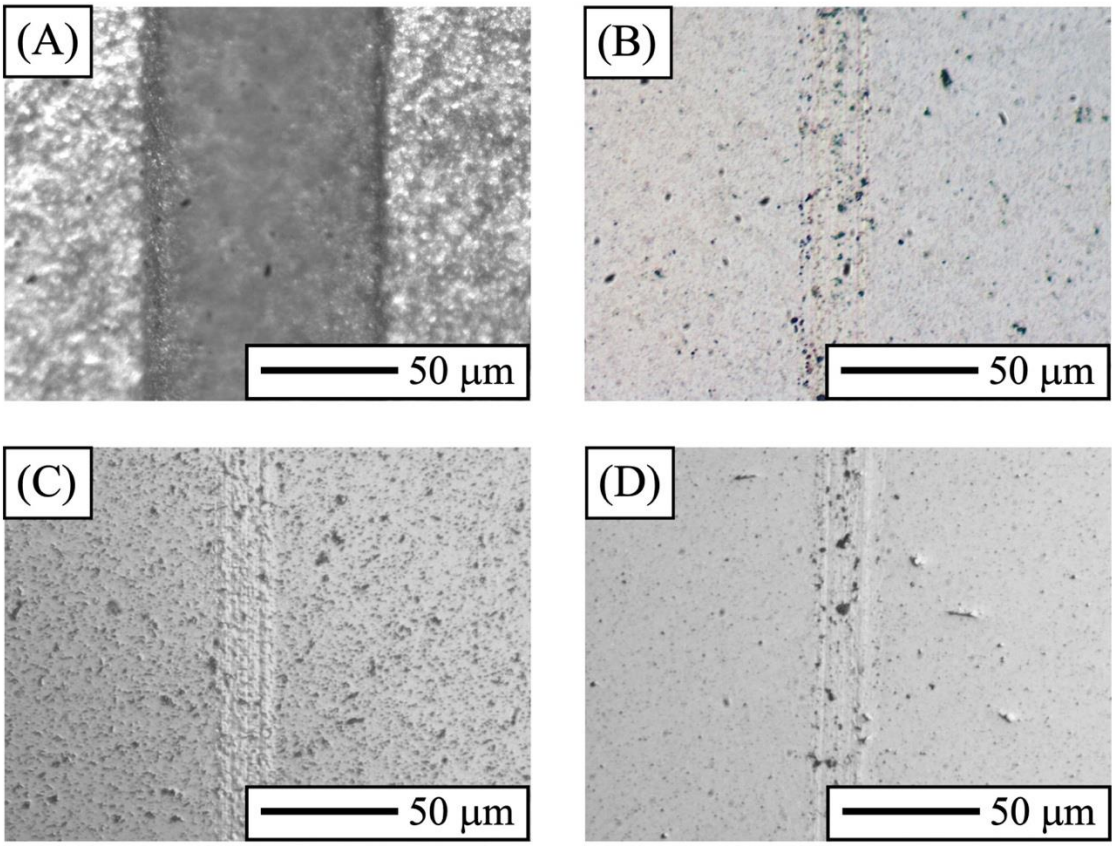

Figure 9. *OM images representative of the scratch tracks in (A) Ref-B_4C-1400°C, (B) Comp-B_4C-20%Si-1400°C, (C) Ref-B_4C-1800°C, and (D) Comp-B_4C-4.28%Si-1800°C.*

Second, small proportions of aids may affect notably the wear behaviour (mode, mechanism, and resistance), and even degrade the wear performance more than a slight residual porosity. Therefore, efforts to achieve the full densification of super- or ultrahard ceramics above a certain porosity threshold may sometimes be unnecessary.

Third, ceramic composites are generally less wear durable than the corresponding monolithic ceramics, attributable to the intrinsic interfacial weakness of the former favouring microcracking-driven material removal. Exceptions to this rule could be ceramic composites with interconnecting phases or extreme anisotropy, where grain removal is difficult, but they require special processing and are thus difficult to scale industrially.

And fourth, greater Vickers hardness is not a guarantee of greater wear resistance, which is attributable to wear being a complex process conditioned, among other factors, by microstructural features. If anything, Vickers hardness might be a good proxy for wear resistance only in the case of purely mechanical wear dominated by plasticity. Models have been developed that consider more static single-cycle mechanical properties (*e.g.*, Vickers hardness, long-crack toughness, and even elastic modulus [43,48-50]), but not microstructural features or the short-crack toughness that is the property pertinent to wear [51]. Moreover, wear is a cumulative multi-cycle process and is not even a material property, but a tribo-system property.

4. Conclusions

A study was conducted of the unlubricated sliding-wear behaviour of B_4C–SiC composites fabricated by SPS from B_4C+Si powders and of their reference B_4C monoliths. Based on the experimental results and analyses, the following conclusions can be drawn:

1. SPS of B_4C+20vol.%Si at only 1400°C results in superhard dense B_4C–SiC composites that

are highly sliding wear resistant, and wear by mild tribo-oxidation with preferential removal of the oxide tribolayer. They are two orders of magnitude more wear resistant than their reference B_4C monoliths, which, due to their very poor sintering, undergo severe microfracture-dominated three-body abrasion.

2. The superhard B_4C–SiC composites SPS-ed at 1400°C from B_4C+20vol.%Si are, despite their lesser hardness and greater proneness to form an oxide tribolayer, only slightly less wear resistant than their ultrahard counterparts SPS-ed at 1800°C from B_4C+4.28vol.%Si, and require a much lower SPS temperature.
3. The B_4C–SiC composites SPS-ed from B_4C+Si are, whether superhard or ultrahard, comparatively a bit less sliding wear resistant than superhard well-sintered B_4C monoliths, attributable to the latter wearing by mild plasticity-dominated two-body abrasion without porosity-induced grain pull-out, but the former require smoother SPS cycles (the more so the more Si aids are used).
4. Vickers hardness is not a reliable guide to screen the wear resistance of the B_4C–SiC composites and B_4C monoliths, attributable to their different wear modes/mechanisms.

Acknowledgements

This work was supported by the Junta de Extremadura under Grants nos. IB20017, TA18014, and GR21170, as well as by the Junta de Andalucía under Grant no. P18-RTJ-1972, all co-financed with FEDER funds.

References

1. P.T.B. Shaffer, Engineering properties of carbides, S.J. Schneider (Ed.), ASTM Engineered Materials Handbook, vol. 4, Ceramics and Glasses, Materials Park, Ohio (1991).
2. F. Thevenot, Boron carbide - a comprehensive review, J. Eur. Ceram. Soc. 6 (4) (1990) 205–225.
3. A.K. Suri, C. Subramanian, J.K. Sonber, T.S.R.-Ch. Murthy, Synthesis and consolidation of boron carbide: a review, Int. Mater. Rev. 55 (1) (2010) 4–40.
4. R.F. Speyer, E.A. Judson, New process makes complex shaped armor a reality, Am. Ceram. Soc. Bull. 85 (3) (2006) 21–23.
5. V. Domnich, S. Reynaud, R.A. Haber, M. Chhowalla, Boron carbide: structure, properties, and stability under stress, J. Am. Ceram. Soc. 94 (11) (2011) 3605–3626.
6. K.Y. Xie, K. Kuwelkar, R.A. Haber, J.C. LaSalvia, K.J. Hemker, Microstructural characterization of a commercial hot-pressed boron carbide armor plate, J. Am. Ceram. Soc. 99 (8) (2016) 2834–2841.
7. Z.L. Chao, T.T. Sun, L.T. Jiang, Z.S. Zhou, G.Q. Chen, Q.Z., G.H. Wu, Ballistic behavior and microstructure evolution of B_4C/AA2024 composites, Ceram. Int. 45 (16) (2019) 20539–20544.
8. Y. Zhang, H. Dong, K. Liang, Y. Huang, Impact simulation and ballistic analysis of B_4C composite armour based on target plate tests, Ceram. Int. 47 (7 Part A) (2021) 10035–10049.
9. X. Yue, M. Huo, J. Liu, J. Wang, H. Ru, Microstructure and properties of bilayered B_4C-based ceramics, J. Eur. Ceram. Soc. 42 (8) (2022) 3404–3414.
10. K.A. Schwetz, L.S. Sigl, J. Greim, H. Knoch, Wear of boron carbide ceramics by abrasive waterjets, Wear 181–183 (Part 1) (1995) 148–155.

11. J.E. Zorzi, C.A. Perottoni, J.A.H. da Jornada, Hardness and wear resistance of B_4C ceramics prepared with several additives, Mater. Lett. 59 (23) (2005) 2932–2935.
12. J. Deng, Erosion wear of boron carbide ceramics nozzles by abrasive air-jets, Mater. Sci. Eng. A 408 (1–2) (2005) 227–233.
13. W. Lin, N. Feng, L. He, Wear properties of reaction sintered B_4C composites, Adv. Mater. Res. 152–153 (2011) 883–886.
14. S. Junlong, L. Changxia, T. Jin, F. Baofu, Erosion behavior of B_4C based ceramic nozzles by abrasive air-jet, Ceram. Int. 38 (8) (2012) 6599–6605.
15. B.M. Moshtaghioun, D. Gómez-García, A. Domínguez-Rodríguez, R.I. Todd, Abrasive wear rate of boron carbide ceramics: influence of microstructural and mechanical aspects on their tribological response, J. Eur. Ceram. Soc. 36 (16) (2016) 3925–3928.
16. A.M. Turatti, A.S. Pereira, Wear resistant boron carbide compacts produced by pressureless sintering, Ceram. Int. 43 (11) (2017) 7970–7977.
17. A.L. Ortiz, V.M. Candelario, O. Borrero-López, F. Guiberteau, Sliding-wear resistance of pure near fully-dense B_4C under lubrication with water, diesel fuel, and paraffin oil, J. Eur. Ceram. Soc. 38 (4) (2018) 1158–1163.
18. M. Bougoin, F. Thevenot, J. Dubois, G. Fantozzi, Synthese et proprietes thermomecaniques de ceramiques denses composites carbure de bore-carbure de silicium, J. Less-Common Met. 132 (2) (1987) 209–228.
19. F. Thevenot, Sintering of boron carbide and boron carbide-silicon carbide two-phase materials and their properties, J, Nucl. Mater 152 (2–3) (1998) 154–162.
20. F.C. Sahin, B. Apak, I. Akin, H.E. Kanbur, D.H. Genckan, A. Turan, G. Goller, O. Yucel, Spark plasma sintering of B_4C-SiC composites, J. Solid State Sci. (14) (2012) 1660–1663.
21. B.M. Moshtaghioun, A.L. Ortiz, D. Gómez-García, A. Domínguez-Rodríguez, Toughening

of super-hard ultra-fine grained B_4C densified by spark-plasma sintering via SiC addition, J. Eur. Ceram. Soc. 33 (8) (2013) 1395–1401.

22. Z. Zhang, X. Du, W. Wang, Z. Fu, H. Wang, Preparation of B_4C–SiC composite ceramics through hot pressing assisted by mechanical alloying, Int. J. Refract. Metals Hard Mater. (41) (2013) 270–275.
23. B.M. Moshtaghioun, D. Gómez-García, A. Domínguez-Rodríguez, High-temperature plastic deformation of spark plasma sintered boron carbide-based composites: The case study of B_4C–SiC with/without graphite (g), J. Eur. Ceram. Soc. 36 (5) (2016) 1127–1134.
24. A. Moradkhani, H. Baharvandi, Mechanical properties and fracture behavior of B_4C-nano/micro SiC composites produced by pressureless sintering, Int. J. Refract. Metals Hard Mater. (70) (2018) 107–115.
25. S.M. So, W.H. Choi, K.H. Kim, J.S. Park, M.S. Kim, J. Park, Y.-S. Lim, H.S. Kim, Mechanical properties of B_4C–SiC composites fabricated by hot-press sintering, Ceram. Int. 46 (7) (2020) 9575–9581.
26. B. Matović, J. Maletaškić, T. Prikhna, V. Urbanovich, V. Girman, M. Lisnichuk, B. Todorović, K. Yoshida, I. Cvijović-Alagić, Characterization of B_4C-SiC ceramic composites prepared by ultra-high pressure sintering, J. Eur. Ceram. Soc. 41 (9) (2021) 4755–4760.
27. B.R. Lawn, N.P. Padture, L.M. Braun, S.J. Bennison, Model for toughness curves in two-phase ceramics: I, basic fracture mechanics, J. Am. Ceram. Soc. 76 (9) (1993) 2235–2240.
28. N.P. Padture, J.L. Runyan, S.J. Bennison, L.M. Braun, B.R. Lawn, Model for toughness curves in two-phase ceramics: II, microstructural variables, J. Am. Ceram. Soc. 76 (9) (1993) 2241–2247.
29. X. Zhang, Z. Zhang, W. Wang, X. Zhang, J. Mu, G. Wang, Z. Fu, Preparation of B_4C composites toughened by TiB_2-SiC agglomerates, J. Eur. Ceram. Soc. 37 (2) (2017) 865–

869.

30. W.S. Rubink, V. Ageh, H. Lide, N.A. Ley, M.L. Young, D.T. Casem, E.J. Faierson, T.W. Scharf, Spark plasma sintering of B_4C and B_4C-TiB_2 composites: deformation and failure mechanisms under quasistatic and dynamic loading, J. Eur. Ceram. Soc. 41 (6) (2021) 3321–3332.
31. J. Dai, E.J. Pineda, B.A. Bednarcyk, J. Singh, N. Yamamoto, Micromechanics-based simulation of B_4C-TiB_2 composite fracture under tensile load, J. Eur. Ceram. Soc. 42 (14) (2022) 6364–6378.
32. C. Ojalvo, F. Guiberteau, A.L. Ortiz, Fabricating toughened super-hard B_4C composites at lower temperature by transient liquid-phase assisted spark plasma sintering with $MoSi_2$ additives, J. Eur. Ceram. Soc. 39 (9) (2019) 2862–2873.
33. V. Zamora, F. Guiberteau, O. Borrero-López, A.L. Ortiz, Ultra-low temperature spark plasma sintering of super wear-resistant hard B_4C composites, Scripta Mater. 211 (2022) 114516.
34. Z.A. Yas, R.A. Haber, Evaluating the role of uniformity on the properties of B_4C–SiC composites, Ceram. Int. 47 (4) (2021) 4838–4844.
35. Z. Zhang, X. Du, Z. Li, W. Wang, J. Zhang, Z. Fu, Microstructures and mechanical properties of B_4C–SiC intergranular/intragranular nanocomposite ceramics fabricated from B_4C, Si, and graphite powders, J. Eur. Ceram. Soc. 34 (10) (2014) 2153–2161.
36. X. Zhang, Z. Zhang, W. Wang, H. Che, X. Zhang, Y. Bai, L. Zhang, Z. Fu, Densification behaviour and mechanical properties of B_4C–SiC intergranular/intragranular nanocomposites fabricated through spark plasma sintering assisted by mechanochemistry, Ceram. Int. 43 (2) (2017) 1904–1910.
37. F. Ye, Z. Hou, H. Zhang, L. Liu, Densification and mechanical properties of spark plasma sintered B_4C with Si as a sintering aid, J. Am. Ceram. Soc. 93 (10) (2010) 2956–2959.

38. S.S. Rehman, W. Ji, S.A. Khan, Z. Fun, F. Zhang, Microstructure and mechanical properties of B_4C densified by spark plasma sintering with Si as a sintering aid, Ceram. Int. 41 (1 Part B) (2015) 1903–1906.

39. L. Ma, K.Y. Xie, M.F. Toksoy, K.Kuwelkar, R.A. Haber, K.J. Hemker, The effect of Si on the microstructure and mechanical properties of spark plasma sintered boron carbide, Mat. Charact. 134 (2017) 274–278.

40. V. Zamora, F.J. Martínez-Vázquez, F. Guiberteau, A.L. Ortiz, Spark-plasma sintering of boron carbide–silicon carbide composites at 1400 °C from B_4C+Si: densification and sintering/reaction mechanisms, J. Eur. Ceram. Soc. (2022), in press.

41. O. Vasiliev, V. Muratov, P. Mazur, V. Bilyi, M. Karpets, V. Bekenev, V. Garbuz, T. Khomko, V. Kartuzov, Silicon in intericosahedra chains of boron carbide, J. Eur. Ceram. Soc. 42 (13) (2022) 5515–5521.

42. B.M. Moshtaghioun, D. Gómez-García, A. Domínguez-Rodríguez, R.I. Todd, Grain size dependence of hardness and fracture toughness in pure near fully-dense boron carbide ceramics, J. Eur. Ceram. Soc. 36 (7) (2016) 1829–1834.

43. B. Bhushan, Modern tribology handbook, CRC Press, Boca Raton, USA, 2001.

44. G. Stachowiak, A.W. Batchelor, Engineering tribology, 3rd Edition, Elsevier Butterworth-Heinemann, Oxford, UK, 2005.

45. C. Ojalvo, E. Sánchez-González, F. Guiberteau, O. Borrero-López, A.L. Ortiz, Improving the dry sliding-wear resistance of B_4C ceramics by transient liquid-phase sintering, J. Eur. Ceram. Soc. 40 (15) (2020) 15286–5292.

46. C. Ojalvo, V. Zamora, R. Moreno, F. Guiberteau, A.L. Ortiz, Transient liquid-phase assisted spark-plasma sintering and dry sliding wear of B_4C ceramics fabricated from B_4C nanopowders, J. Eur. Ceram. Soc. 41 (3) (2021) 1869–1877.

47. V. Zamora, C. Ojalvo, F. Guiberteau, O. Borrero-López, A.L. Ortiz, Ultra-low wear B_4C–SiC–MoB_2 composites fabricated at lower temperature from B_4C with $MoSi_2$ additives, J. Eur. Ceram. Soc. 41 (16) (2021) 68–75.

48. B.R. Lawn, H. Huang, M. Liu, O. Borrero-Lopez, Y. Zhang, Threshold damage mechanisms in brittle solids and their impact on advanced technologies, Acta Mater. 232 (2022) 117921.

49. A.G. Evans, T.R. Wilshaw, Quasi-static solid particle damage in brittle solids, I. Observations, analysis and implications, Acta Metal. 24 (10) (1976) 939–956.

50. A.G Evans, D.B. Marshall, Wear mechanism in ceramics, in Fundamental of friction and wear of materials (ed . D.A. Rigney), ASM, Metals Park, Ohio (1980).

51. X. Wang, N.P. Padture, H. Tanaka, A.L. Ortiz, Wear-resistant ultra-fine-grained ceramics, Acta Mater. 53 (2) (2005) 271–277.

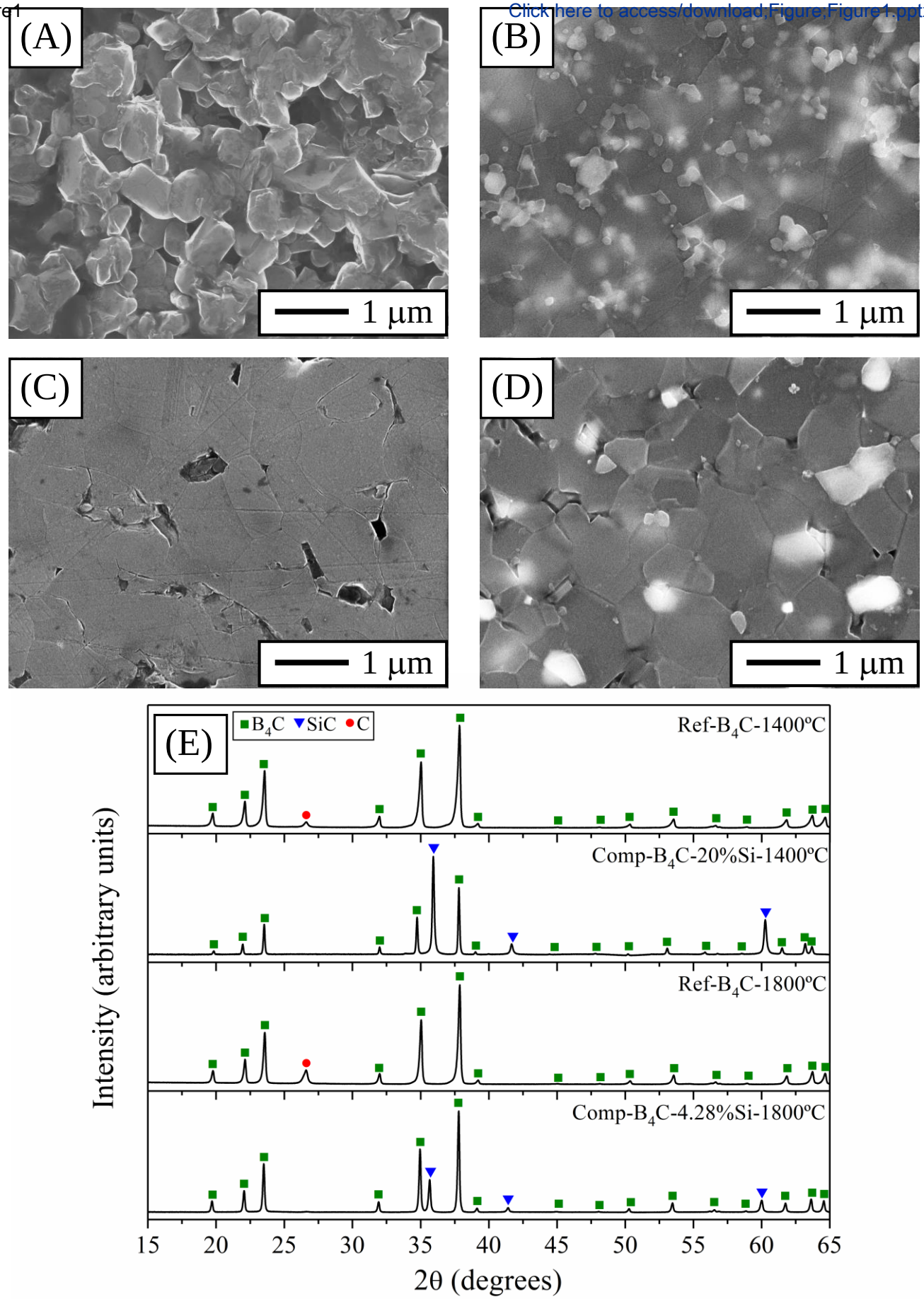

Figure 1

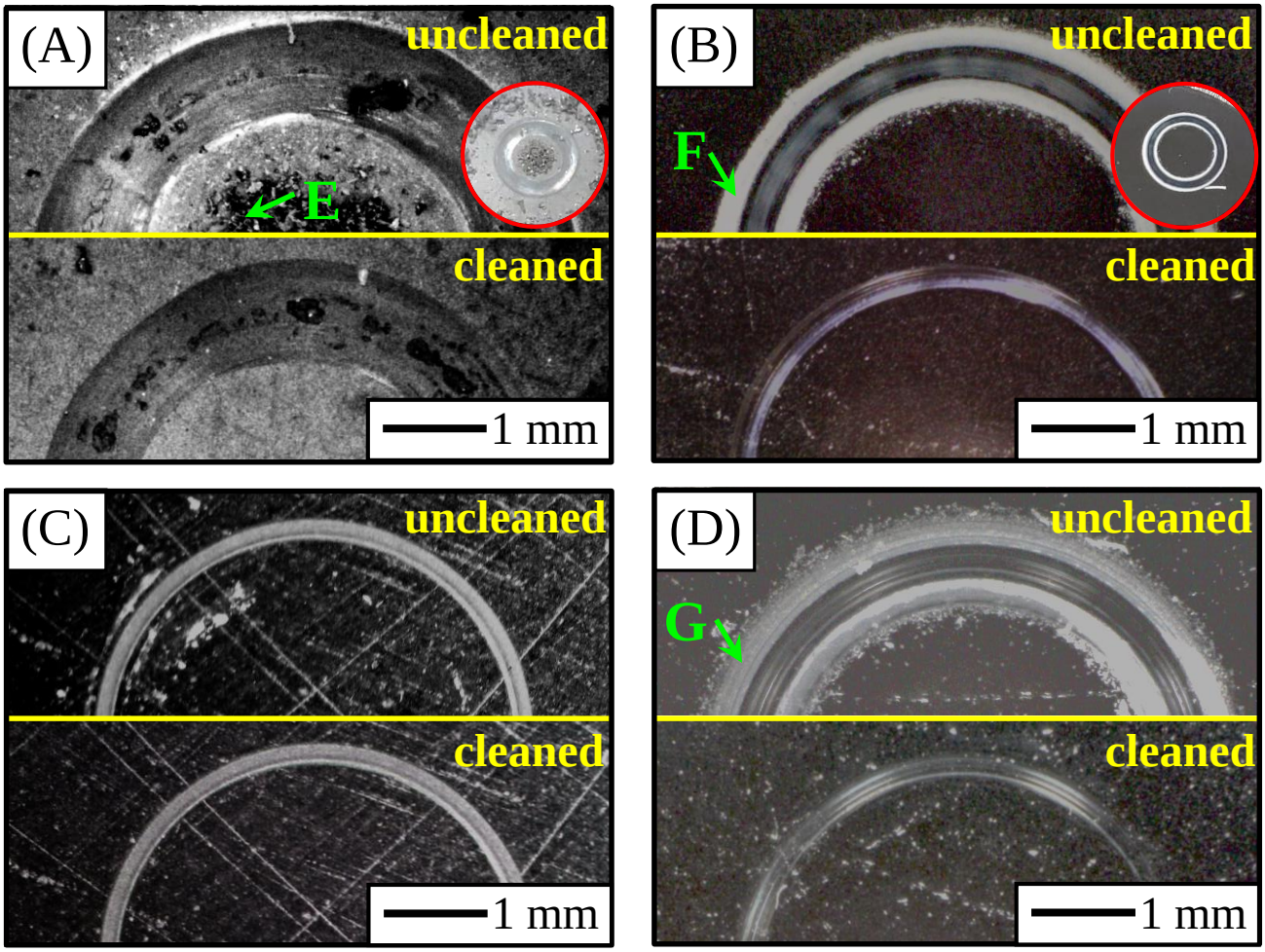

Figure 2

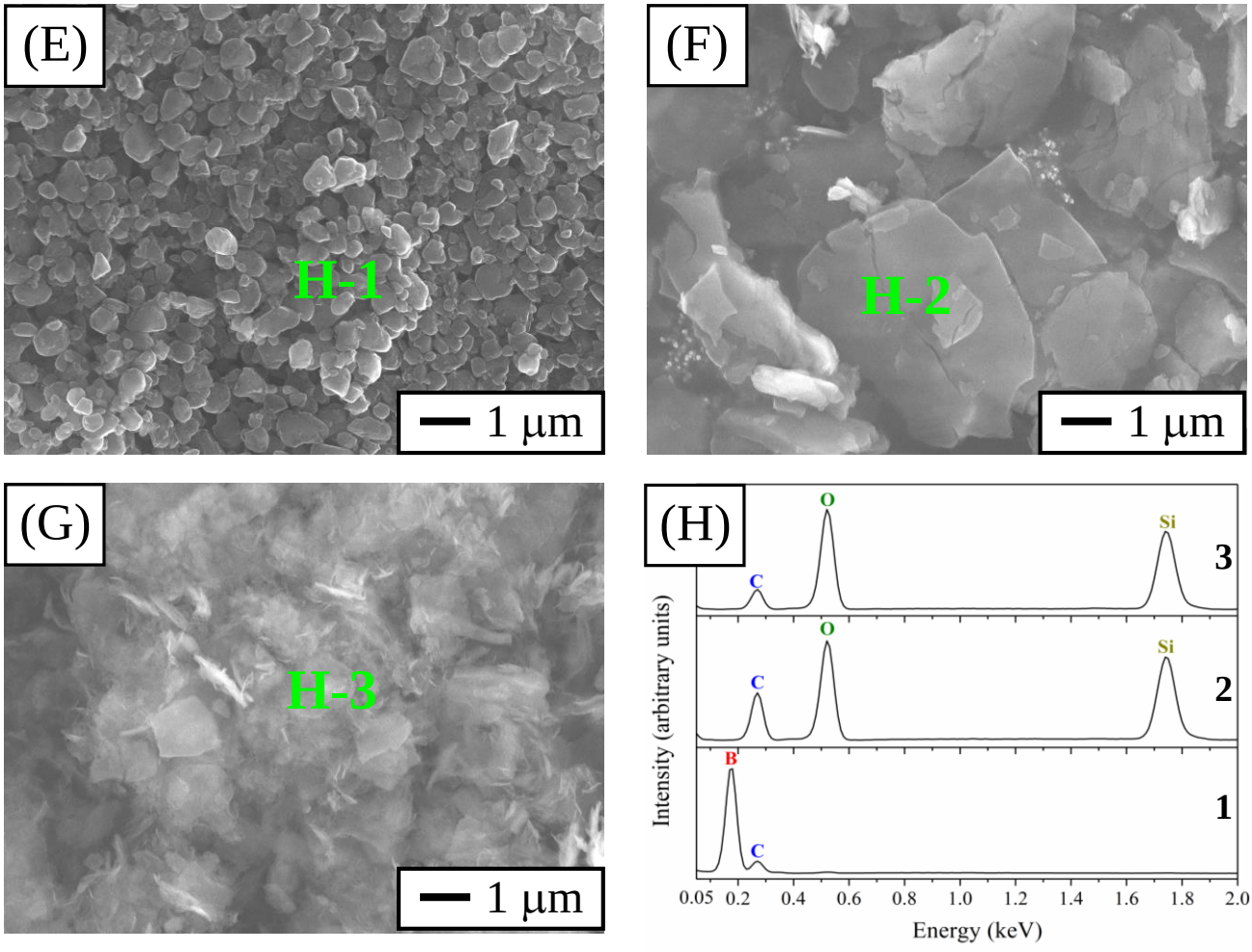
(E)
H-1
1 μm
(F)
H-2
1 μm
(G)
H-3
1 μm
(H)
O
Si
C
3
O
Si
C
2
B
C
1
Intensity (arbitrary units)
0.05 0.2 0.4 0.6 0.8 1.0 1.2 1.4 1.6 1.8 2.0
Energy (keV)

Figure 2

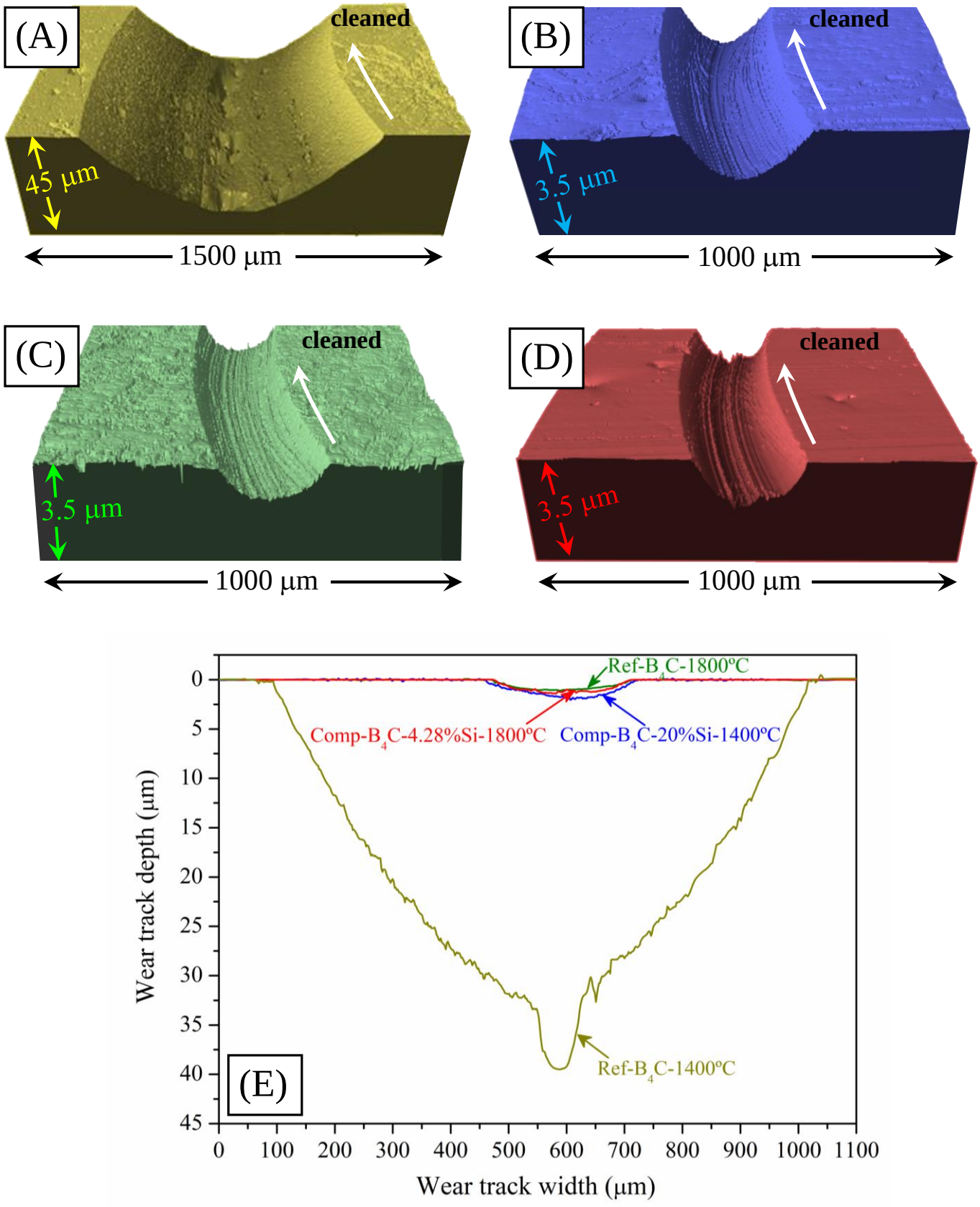

Figure 3

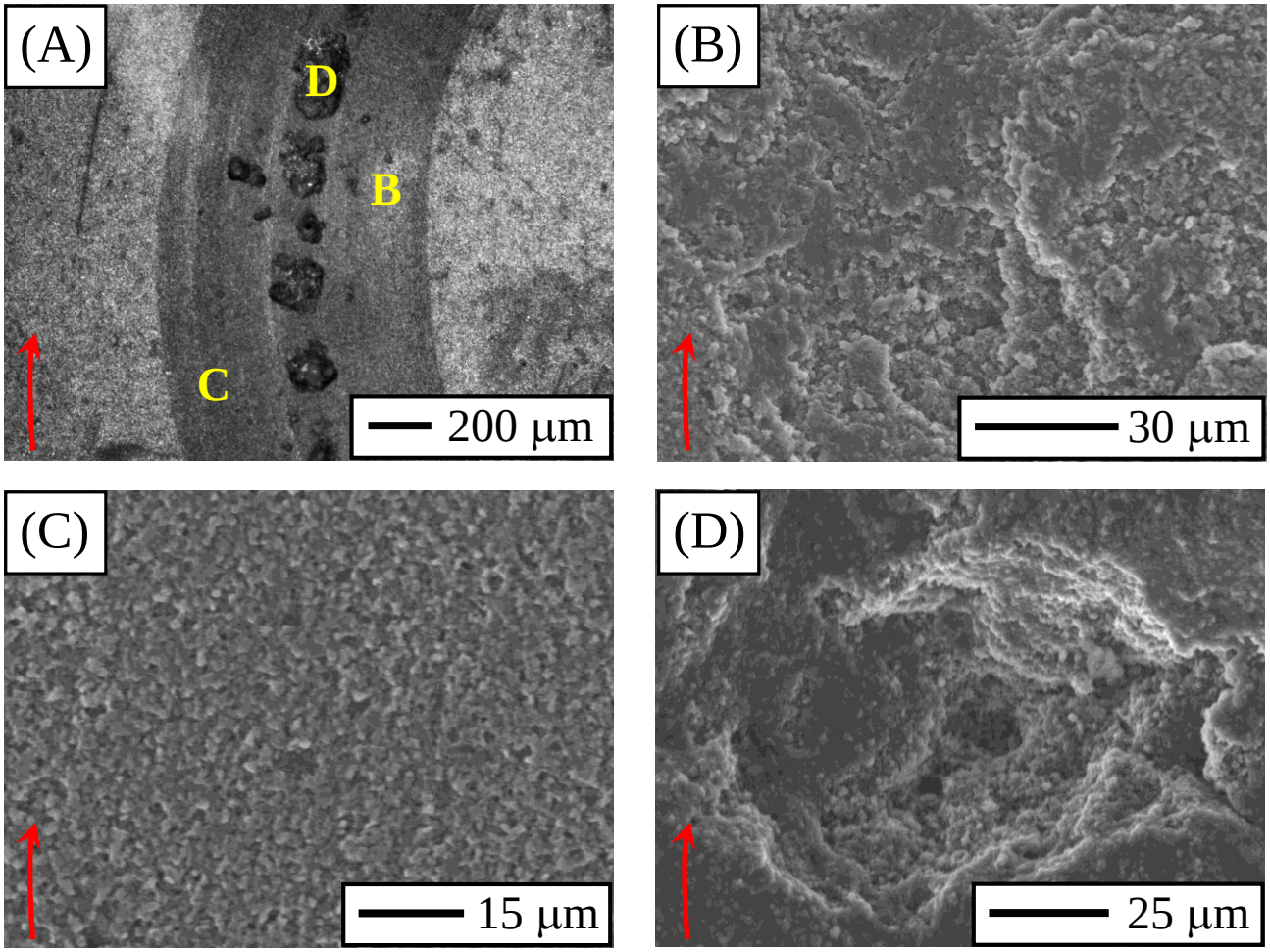

Figure 4

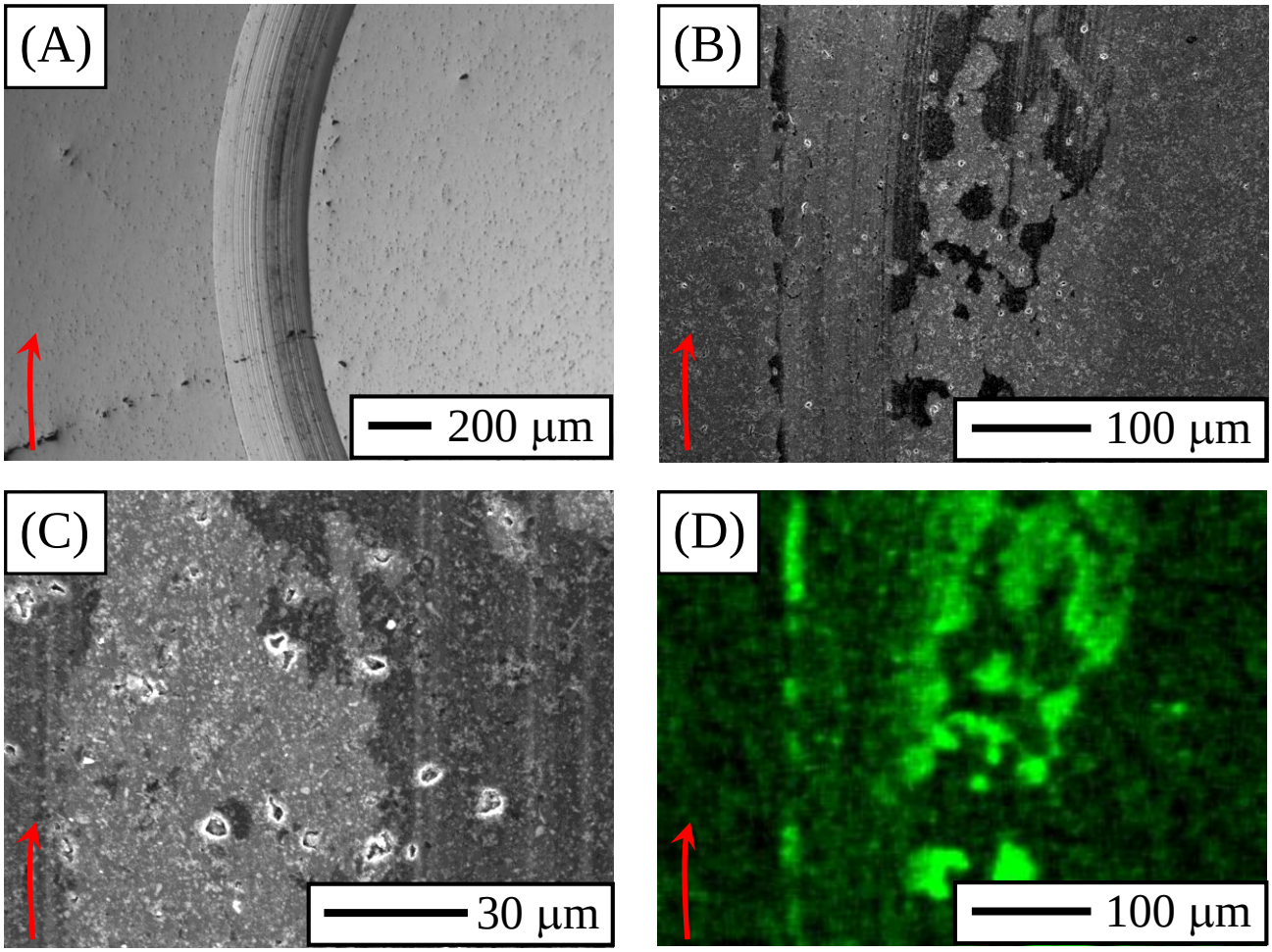

Figure 5

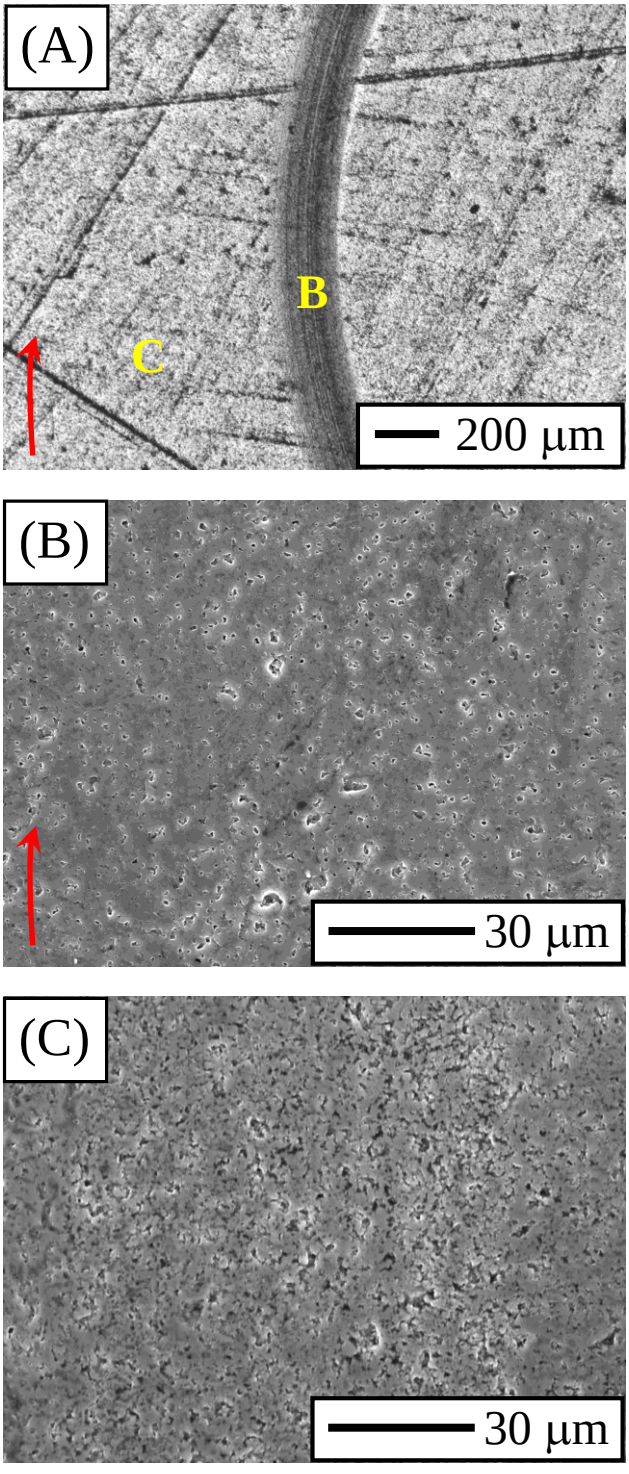

Figure 6

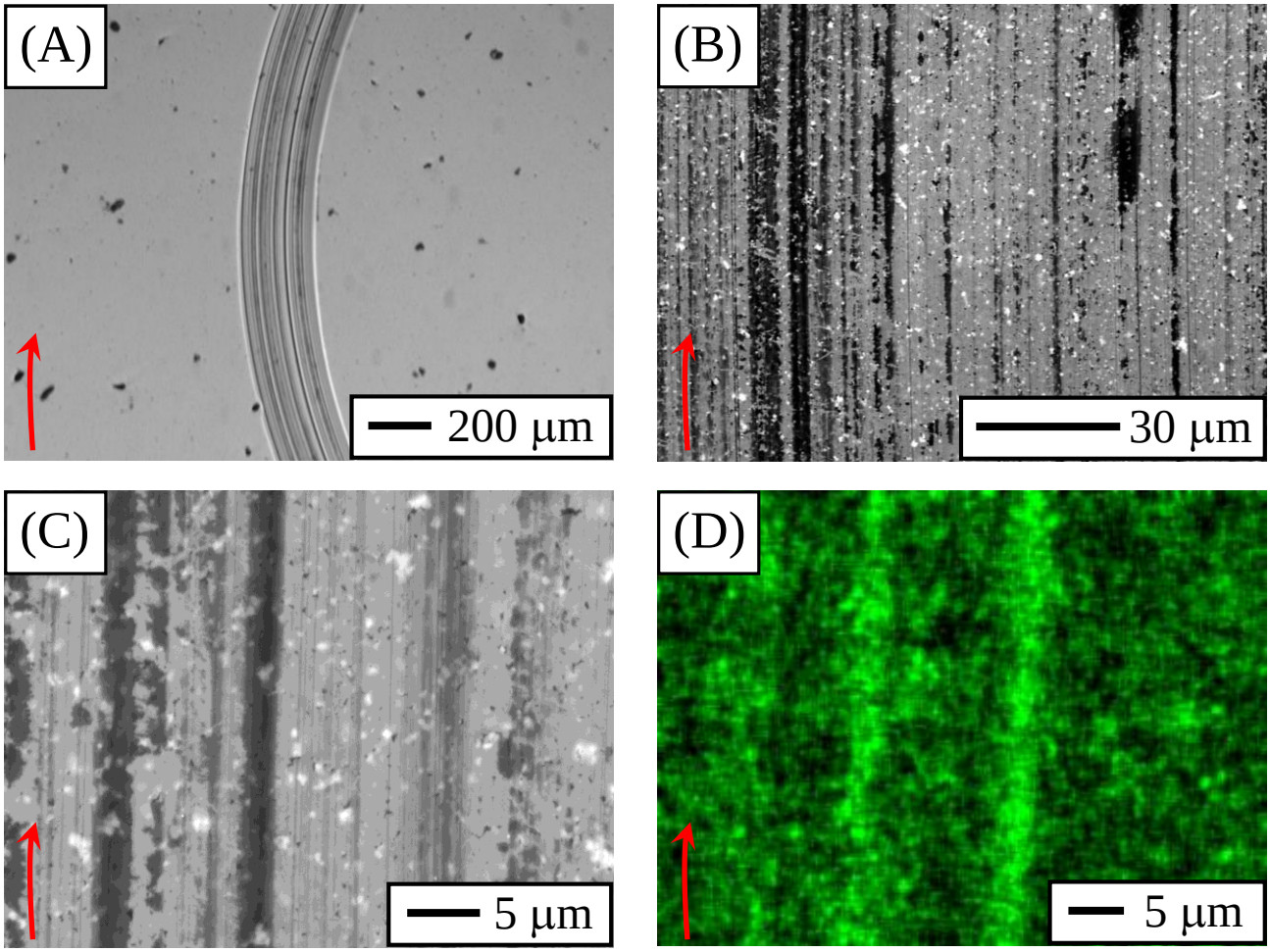

Figure 7

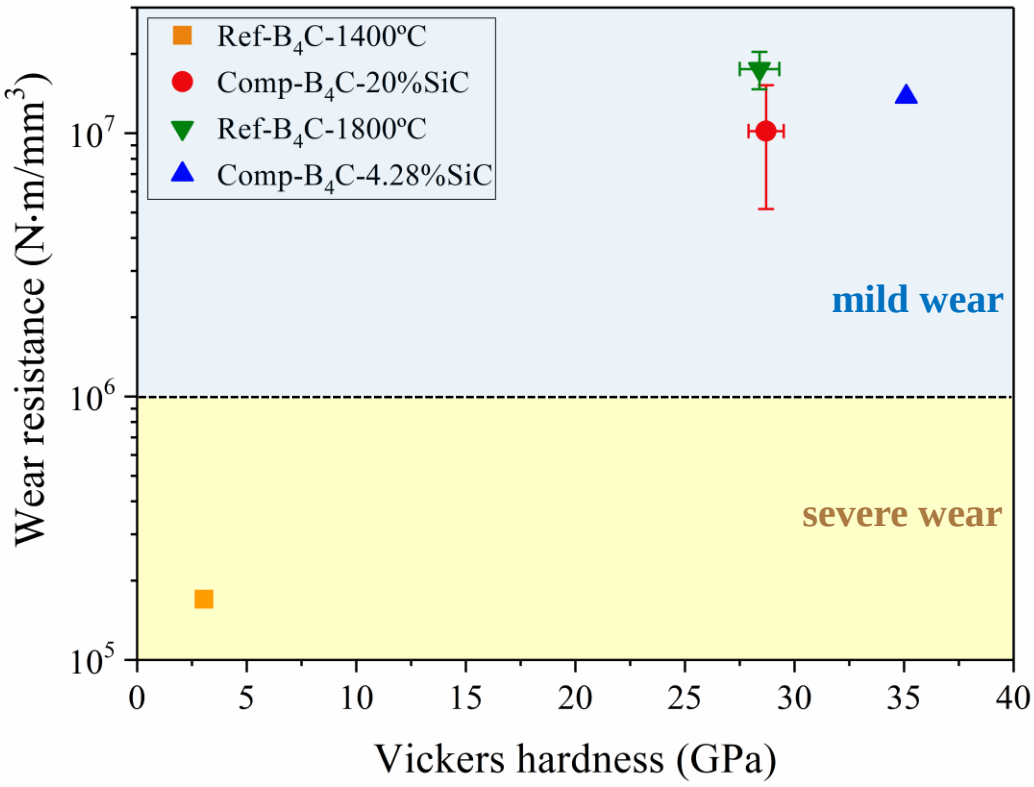

Figure 8

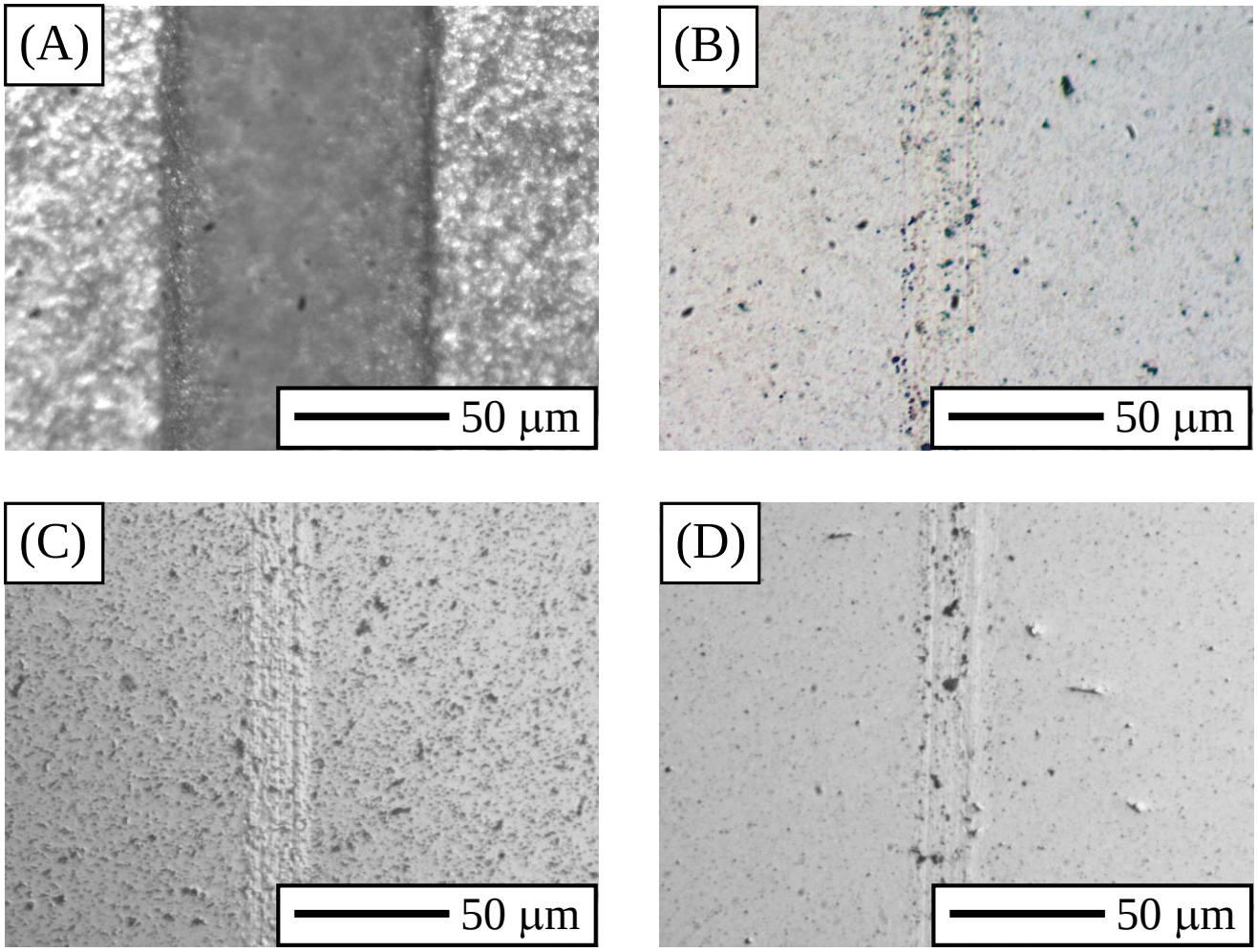

Figure 9

Figure Captions

Figure 1. SEM images representative of the polished, electrochemically etched (1% KOH solution at ~0.03 A/cm² for ~30 s) surface of (A) Ref-B_4C-1400°C, (B) Comp-B_4C-20%Si-1400°C, (C) Ref-B_4C-1800°C, and (D) Comp-B_4C-4.28%Si-1800°C, as well as (E) XRD patterns of these four materials, as indicated. The SEM imaging was done with secondary electrons at 15 kV. In (B) and (D), dark-grey grains are boron carbide and white grains are β-SiC. The XRD patterns were acquired with pure $CuK\alpha_1$ incident radiation, and were indexed using the PDF2 database. The weak C peak in the XRD patterns of Ref-B_4C-1400°C and Ref-B_4C-1800°C indicates a very minor content (*i.e.*, <1 wt.%) of residual C (impurity of the B_4C and/or taken up during SPS).

Figure 2. DOM images representative of the uncleaned (top) and cleaned (bottom) wear tracks of (A) Ref-B_4C-1400°C, (B) Comp-B_4C-20%Si-1400°C, (C) Ref-B_4C-1800°C, and (D) Comp-B_4C-4.28%Si-1800°C at the conclusion of the wear tests (*i.e.*, 1000 m slid). The insets in (A) and (B) show lower-magnification DOM images of the entire wear track (4-cm diameter). SEM images of the wear debris collected from (E) Ref-B_4C-1400°C, (F) Comp-B_4C-20%Si-1400°C, and (G) Comp-B_4C-4.28%Si-1800°C, as well as (H) the corresponding indexed EDS spectra. The SEM imaging was done with secondary electrons at 20 kV, and EDS analyses at 10 kV. The letters E, F, G, H1, H2, and H3 correlate images with each other.

Figure 3. OP 3-D images representative of the cleaned wear tracks of (A) Ref-B_4C-1400°C, (B) Comp-B_4C-20%Si-1400°C, (C) Ref-B_4C-1800°C, and (D) Comp-B_4C-4.28%Si-1800°C at the conclusion of the wear tests (*i.e.*, 1000 m slid), as well as (E) typical 2-D profiles extracted from them, as indicated. The white arrows in (A)-(D) denote the sliding direction.

Figure 4. (A) OM and (B-D) SEM images showing the wear damage at the macro- and micro-scales in Ref-B_4C-1400°C at the conclusion of the wear tests (*i.e.*, 1000 m slid) after cleaning the worn surface. SEM imaging was done with secondary electrons at 15 kV. The red arrows denote the sliding direction. The letters B, C, and D in (A) correlate images with each other.

Figure 5. (A) OM and (B-C) SEM images representative of the wear damage at the macro- and micro-scales in Comp-B_4C-20%Si-1400°C at the conclusion of the wear tests (*i.e.*, 1000 m slid) after cleaning the worn surface. (D) EDS elemental composition map of O inside and outside the wear track. SEM imaging was done with secondary electrons at 15 kV, and EDS mapping also at 15 kV. The red arrows denote the sliding direction.

Figure 6. (A) OM and (B) SEM image representative of the wear damage at the macro- and micro-scales in Ref-B_4C-1800°C at the conclusion of the wear tests (*i.e.*, 1000 m slid) after cleaning the worn surface. (C) SEM image representative of the surface of Ref-B_4C-1800°C outside the wear track showing that the pitted zones in (B) consist of pores, not grains pulled-out during the wear tests. SEM imaging was done with secondary electrons at 15 kV. The red arrows in (A)-(B) denote the sliding direction.

Figure 7. (A) OM and (B-C) SEM images representative of the wear damage at the macro- and micro-scales in Comp-B_4C-4.28%Si-1800°C at the conclusion of the wear tests (*i.e.*, 1000 m slid) after cleaning the worn surface. (D) EDS elemental composition map of O inside the wear track. SEM imaging was done with secondary electrons at 15 kV, and EDS mapping also at 15 kV. The red arrows denote the sliding direction.

Figure 8. Wear resistance of Ref-B_4C-1400°C, Comp-B_4C-20%Si-1400°C, Ref-B_4C-1800°C, and Comp-B_4C-4.28%Si-1800°C as a function of their Vickers hardness, as indicated. The regimes of severe and mild wear are distinguished.

Figure 9. OM images representative of the scratch tracks in (A) Ref-B_4C-1400°C, (B) Comp-B_4C-20%Si-1400°C, (C) Ref-B_4C-1800°C, and (D) Comp-B_4C-4.28%Si-1800°C.

- SPS of B_4C+20vol.%Si at 1400°C yields highly wear resistant B_4C–SiC composites.
- SPS of B_4C+4.28vol.%Si at 1800°C yields even more wear resistant B_4C–SiC composites.
- The B_4C–SiC composites SPS-ed from B_4C+Si wear by mild tribo-oxidation with preferential removal of the tribolayer.
- The reference B_4C monoliths SPS-ed at 1400°C undergo severe wear by mechanical abrasion.
- The reference B_4C monoliths SPS-ed at 1800°C undergo mild wear by mechanical abrasion.
- Superhard B_4C monoliths are more sliding wear resistant than superhard/ultrahard B_4C–SiC composites.